

COSMOLOGICAL DISTANCE MEASUREMENT OF 12 NEARBY SUPERNOVAE IIP WITH ROTSE-IIIB

G. DHUNGANA^{1,*}, R. KEHOE¹, R. STATEN¹, J. VINKO^{2,3,4,5}, J. C. WHEELER², C. AKERLOF⁶, D. DOSS⁷, F. V. FERRANTE¹,
C. A. GIBSON⁷, J. LASKER¹, G. H. MARION², S. B. PANDEY⁸, R. M. QUIMBY^{9,10}, E. RYKOFF¹¹, D. SMITH¹², F. YUAN⁶,
AND W. ZHENG^{6,11}

Draft version August 7, 2023

ABSTRACT

We present cosmological analysis of 12 nearby ($z < 0.06$) Type IIP supernovae (SNe IIP) observed with the ROTSE-IIIB telescope. To achieve precise photometry, we present a new image differencing technique that is implemented for the first time on the ROTSE SN photometry pipeline. With this method, we find up to a 20% increase in the detection efficiency and significant reduction in residual RMS scatter of the SN lightcurves when compared to the previous pipeline performance. We use the published optical spectra and broadband photometry of well studied SNe IIP to establish temporal models for ejecta velocity and photospheric temperature evolution for our SNe IIP population. This study yields measurements that are competitive to other methods even when the data are limited to a single epoch during the photospheric phase of SNe IIP. Using the fully reduced ROTSE photometry and optical spectra, we apply these models to the respective photometric epochs for each SN in the ROTSE IIP sample. This facilitates the use of the Expanding Photosphere Method (EPM) to obtain distance estimates to their respective host galaxies. We then perform cosmological parameter fitting using these EPM distances from which we measure the Hubble constant to be $72.9^{+5.7}_{-4.3}$ $\text{kms}^{-1} \text{Mpc}^{-1}$, which is consistent with the standard ΛCDM model values derived using other independent techniques.

Subject headings: supernovae: general — galaxies: cosmology, distances and redshifts — photometry: general — spectroscopy: general

1. INTRODUCTION

Supernova (SN) cosmology has matured over the past few decades. Supernovae (SNe) have proven excellent distance indicators for astronomy and cosmology due to their enormous and standardizable intrinsic brightness. Specifically, the improvements in the methods to precisely calibrate distances using the luminosities of SNe Ia

remain in the forefront of SN cosmology. With the arrival of deeper surveys, these methods are being tested at even higher redshifts, and will prove complementary to other high redshift cosmological probes such as baryon acoustic oscillations (BAO), cosmic microwave background (CMB), and weak lensing (see Weinberg et al. (2013); Nicola et al. (2017) for a review). While SNe Ia yield remarkable precision for the distance calibration based on their peak luminosity and light curve width relation (e.g. Phillips (1993); Tripp (1998); Riess et al. (1998); Perlmutter et al. (1999); DES Collaboration et al. (2018); Brout et al. (2022)), there remain questions about potential impact of discrepancies between the SN Ia models and the actual physical processes occurring (Benetti et al. 2005; Howell 2011; Marion et al. 2016; Blondin et al. 2017).

SNe IIP are continuously gaining interest as a standardizable candle population that provides a potent alternative class of distance indicators. The SNe IIP are believed to arise from the catastrophic gravitational collapse of the iron core of massive stars that have retained a substantial hydrogen envelope even at the time of collapse (e.g. Branch & Wheeler (2017) Ch. 12). Because the explosion mechanism as well as the radiative transfer in SNe IIP are believed to be better understood than SNe Ia, the distance estimation is expected to be less affected by the systematic uncertainties due to explosion physics (e.g. Eastman, Schmidt & Kirshner (1996)). While SNe Ia may exhibit higher absolute luminosity, SNe IIP explosions also offer tremendous luminosity and are more

¹ Department of Physics, Southern Methodist University, Dallas, TX, USA

² Department of Astronomy, University of Texas at Austin, 2515 Speedway, Stop C1400, Austin, Texas 78712-1205

³ CSFK Konkoly Observatory, Budapest, Konkoly-Thege M. ut 15-17, 1121, Hungary

⁴ Department of Optics and Quantum Electronics, University of Szeged, Dom ter 9, Szeged, 6720 Hungary

⁵ ELTE Eötvös Loránd University, Institute of Physics, Pázmány Péter stány 1/A, Budapest, 1117 Hungary

⁶ Department of Physics, University of Michigan, Ann Arbor, MI, USA

⁷ McDonald Observatory, University of Texas at Austin, TX, USA

⁸ Aryabhata Research Institute of Observational Sciences (ARIES), Manora Peak, Nainital, Uttarakhand, India, 263001

⁹ Department of Astronomy/Mount Laguna Observatory, San Diego State University, 5500 Campanile Drive, San Diego, CA, USA

¹⁰ Kavli Institute for the Physics and Mathematics of the Universe (WPI), The University of Tokyo Institutes for Advanced Study, The University of Tokyo, Kashiwa, Chiba 277-8583, Japan

¹¹ Department of Astronomy, University of California, Berkeley, California, USA

¹² Guilford College, USA

* gdhungana@smu.edu

frequently occurring than SNe Ia (e.g. (Graur et al. 2015)), presenting themselves as competitive distance indicators over an extensive redshift baseline. While these SNe show substantial diversity in their photometric and spectroscopic properties (Filippenko 1997; Hatano et al. 1999; Faran et al. 2014; Dhungana et al. 2016; Valenti et al. 2016; Branch & Wheeler 2017), strong correlations in photometric and spectroscopic observables during the recombination phase can be exploited to provide a distance calibration. Several methods have been proposed over the last few decades to make the SNe IIP distance measurements calibratable. These methods are generally driven by the correlations of the luminosity with the expansion velocities. The pioneering work of Kirshner & Kwan (1974) using the Expanding Photosphere Method (EPM) treated SN IIP as a homologously expanding photosphere that emits light as a blackbody diluted from atmospheric scattering. This method relies on both the photometry and spectroscopy, where the observed flux is compared to the effective blackbody flux in the SN rest frame during the photospheric expansion phase of the SNe IIP. Using the models for the dilution correction factor (e.g. Dessart & Hillier (2005); Eastman, Schmidt & Kirshner (1996)), the EPM technique has been applied to numerous SNe IIP from independent samples (e.g Schmidt et al. (1994); Hamuy et al. (2001); Jones et al. (2009); Vinkó et al. (2012); Bose & Kumar (2014); Dhungana et al. (2016); Gall et al. (2016)). A close variant based on the correlations of luminosity with the expansion velocity at 50d after explosion was suggested and used as the Standardized Candle Method (SCM) (e.g Hamuy & Pinto (2002); Nugent et al. (2006); Poznanski et al. (2010); D’Andrea et al. (2010); de Jaeger et al. (2017); Gall et al. (2018); Vogl et al. (2019); Van Dyk et al. (2019); Szalai et al. (2019); Dong et al. (2021)). The method has been further generalized (e.g. Kasen & Woosley (2009)) to all epochs in the photospheric phase of the events. A newer technique called the Photospheric Magnitude Method (e.g Rodríguez et al. (2014)) is based on empirical color based calibrations for the distance. Rodríguez et al. (2019) used the PMM technique in the near-IR bands where the effects from the dust and line contamination is much smaller compared to the optical wavelengths. de Jaeger et al. (2015) suggested a purely photometric technique called Photometric Color Method (PCM) that requires no spectroscopy unlike previous techniques.

It is important to test and improve these methods as we discover more SNe IIP at higher redshifts. These studies involving limited samples of SNe IIP at lower redshifts show promising signs of them providing independent and competitive distance estimates.

We present a cosmological analysis using distances of 12 SNe IIP that were observed by the ROTSE-III telescopes during the 2004-2013 survey period. Distances are derived using the EPM technique and primarily based only on ROTSE photometry and coordinated optical spectroscopy. This paper is organized as follows. In Section 2, we describe the photometric and spectroscopic data obtained for our SNe IIP sample. Section 3 describes the data reduction based on a new, improved image differencing technique, along with photometric calibrations, spectroscopy and k -corrections. In Section 4, we summarize the mathematical framework for the EPM.

Section 5 discusses the photometric and spectroscopic parameters for the EPM and establishes their time evolution models. The EPM distance measurements are discussed in Section 6. Section 7 presents the cosmological analysis and the Hubble diagram for our SNe IIP sample. We present the results and discussion in Section and finally our conclusions from the paper in Section 9.

2. OBSERVATIONS

2.1. Photometry

Photometric observations were obtained by the ROTSE-IIIb telescope at McDonald Observatory (Akerlof et al. 2003). The ROTSE-III instruments are 0.45 m robotic Cassegrain telescopes with a $1.85^\circ \times 1.85^\circ$ field of view (FOV). They operate with an unfiltered $2k \times 2k$ pixel back-illuminated CCD with broad transmission over a wavelength range of $3,000 - 10,000 \text{ \AA}$, achieving a typical limiting magnitude of ~ 18 mag.

A sample of 12 SNe IIP is obtained from the ROTSE Supernova Survey comprised of three SN search programs spanning from 2004 to 2013. A summary table of the 12 events with their host galaxies is given in Table 1. Each event in this sample has multiple photometric measurements between 1 week and 5 weeks after explosion. We will discuss below why this time range is suited for the EPM technique using SNe IIP. This sample constituted 4 events from Texas Supernova Search (TSS) (Quimby (2006)), 5 events from ROTSE Supernova Verification Project (RSVP) (Yuan (2010)) and 3 events from Texas Supernova Spectroscopic Survey (TS³) (Dhungana (2018)). The TSS survey involved the northern sky survey using the ROTSE - IIIb telescope with nightly patrol of thousands of galaxies in the nearby clusters. The TSS aimed at amassing a small collection of well observed SNe, targeting the earliest possible photometric observation and likewise a triggered spectroscopic followup with the nearby Hobby Eberly Telescope (HET). The RSVP survey extended the northern sky with more fields using both the ROTSE- IIIb and IIIc telescopes, along with the southern sky coverage using the IIIa and IIIc telescopes. The TS³ survey continued with the RSVP fields in automated survey mode, however, new triggered follow up photometric and spectroscopic observations were also added for the interesting events within and outside the existing ROTSE footprint. For most of the survey fields, the ROTSE observations are scheduled for a paired successive one minute exposure imaging 30 minutes apart. This scheduling is repeated 2-3 times separated by ~ 2 hours. The follow-up auxiliary fields are generally scheduled using the same scheme apart from a few interesting events where imaging cadence is increased. In the sample of 12 SNe IIP, 6 were discovered by the ROTSE telescopes, 5 others were observed in the regular survey mode and 1 was observed in triggered auxiliary mode.

2.2. Spectroscopy

When available, spectroscopic observations were obtained by the Hobby Eberly Telescope (HET) at McDonald Observatory (Hill et al. 1998). The HET possesses a 9.2 m aperture with a 4 arcmin FOV, using a 3072×1024 pixel CCD. The Low Resolution Spectrograph (LRS) is a high throughput optical ($\sim 4,200 - 10,100 \text{ \AA}$) grism spectrograph attached to the HET tracker, with resolv-

TABLE 1
ROTSE IIP SAMPLE FOR THE EPM STUDY

SN	Program/ROTSE Field	Host Galaxy	Spectra	z	$E(B-V)_{tot}$	Adopted t_0 (MJD)	References
SN 2004gy	TSS/skc1307+2626	NGP9 F379-0005009	1	0.02690 ± 0.00100	0.0100 ± 0.0007	53362.5 ± 2.5	1
SN 2005ay	TSS/tss1152+4327	NGC 3938	3	0.00270 ± 0.00001	0.0183 ± 0.0002	53452.5 ± 4.0	2,3
SN 2006bj	TSS/tss1220+0756	SDSS J122219.09+073725.5	1	0.03770 ± 0.00100	0.0200 ± 0.0004	53815.3 ± 3.0	4
SN 2006bp	TSS/tss1159+5136	NGC 3953	4	0.00351 ± 0.00001	0.4000 ± 0.0100	53833.7 ± 2.0	5,6
SN 2008bj	RSVP/sks1155+4643	MCG +08-22-20	1	0.01896 ± 0.00011	0.0260 ± 0.1000	54534.0 ± 2.5	4
SN 2008gd	RSVP/sks0117+1352	SDSS J012044.48+144139.6	1	0.059096 ± 0.000053	0.2823 ± 0.0582	54726.9 ± 3.5	4
SN 2008in	RSVP/tss1224+0440	NGC 4303	3	0.00522 ± 0.00001	0.1000 ± 0.1000	54825.1 ± 2.1	6,7
SN 2009dd	RSVP/tss1209+4958	NGC 4088	3	0.00252 ± 0.00001	0.3670 ± 0.0070	54928.1 ± 1.3	8
PTF10gva	RSVP/tss1225+1112	SDSS J122355.39+103448.9	1	0.02753 ± 0.00012	0.0263 ± 0.0008	55320.3 ± 0.9	9
SN 2013ab	TS ³ /vsp1443+0953	NGC 5669	2	0.00456 ± 0.00001	0.044 ± 0.066	56339.5 ± 1.0	10
SN 2013bu	TS ³ /skt2237+3425	NGC 7331	1	0.002722 ± 0.000004	0.078 ± 0.0006	56399.3 ± 1.0	11
SN 2013ej	TS ³ /rqa0137+1547	NGC 0628/M74	5	0.00219 ± 0.000003	0.0610 ± 0.0010	56496.9 ± 0.3	12

References: ¹ Guillochon et al. (2017) ² Gal-Yam et al. (2008) ³ Poznanski et al. (2010)

⁴ Kelly & Kirshner (2012) ⁵ Quimby et al. (2007) ⁶ Bose & Kumar (2014) ⁷ Roy et al. (2011)

⁸ Pejcha & Prieto (2015) ⁹ Khazov et al. (2016) ¹⁰ Bose et al. (2015) ¹¹ Valenti et al. (2016) ¹² Dhungana et al. (2016)

ing power of $R = \frac{\lambda}{\Delta\lambda}$ ranging from 600 to 3,000.

Spectra for the SNe IIP sample that were obtained by the HET are archived in the WISEREP (Yaron & Gal-Yam (2012)) catalog. For the events for which no HET spectrum is available, we obtain them from the literature, WISEREP or Open Supernova Catalog (Guillochon et al. (2017)).

3. DATA REDUCTION

3.1. Photometry

ROTSE III photometry is carried out using standard techniques ((Yuan & Akerlof 2008; Dhungana et al. 2016)). The online SN pipeline tasked with prompt analysis and SN discovery utilizes the image differencing software developed for the RSVP (Yuan & Akerlof (2008)). While this differencing is robust for the cases where the SN lies substantially out of the host core, we have sought to improve the detection efficiency and the root mean square (RMS) scatter when the observation is photon limited or close to the host core. Therefore, we developed a new image differencing software which we utilized in the offline ROTSE SN photometric data reduction pipeline.

3.1.1. Image Differencing Technique: Kernel convolution

Image differencing is a common technique used to monitor and characterize the time domain variability of astronomical objects. Because of the variation of observational components across exposures, the exact nature of variability from the astrophysical source requires proper extraction by correctly modeling the backgrounds in each exposure and matching the point spread functions (PSFs). Precise measurements of variability have been performed using differencing technique in various circumstances (Alard & Lupton (1998); Bramich (2008); Kessler et al. (2015)). We present a new differencing software for the ROTSE SN photometry analysis based on the kernel convolution technique (e.g. Alard & Lupton (1998); Becker et al. (2012)). Due to the complexity of the bright background host with an extended PSF, the subtraction technique can yield photometric artifacts. ROTSE was designed to quickly image the large sky areas, thereby maximizing the sky coverage at the cost of spatial resolution. The pixel size of $\sim 1.5''$ is large on the scale of host galaxy morphology. It is also challenging to get an accurate measurement of the signal at the noise limit. Allowing a sufficiently large basis of PSF variation, this

subtraction software, `ImageDiff`¹⁴, attempts to achieve better performance on the ROTSE image differencing, not only when the background is complicated but also when the signal is photon limited.

Given a recent survey(science) image $S(x, y)$, a higher signal-to-noise template image $T(x, y)$, usually prepared by stacking several past images, and a kernel basis $K(u, v)$, the survey image is modeled in a linear combination of kernel convoluted template as

$$S(x, y) = (K \otimes T)(x, y) + \epsilon(x, y) \quad (1)$$

Here, x, y are pixel coordinates and u, v are kernel coordinates, $\epsilon(x, y)$ is the error term. The kernel basis set constitutes i basis kernels, i.e. $K(u, v) = \{k_i(u, v)\}$. We can write Eq. 1 as a linear equation

$$S = \sum_i A_i c_i + \epsilon \quad (2)$$

where, $A_i = k_i \otimes T$ and c_i are the coefficients for the linear combination. We intend to find these coefficients c_i corresponding to each kernel k_i . Assuming Gaussian errors, the maximum likelihood (minimum χ^2) solution for the coefficient matrix will be

$$\mathbf{C} = (\mathbf{A}^T \mathbf{N}^{-1} \mathbf{A})^{-1} \mathbf{A}^T \mathbf{N}^{-1} \mathbf{S} \quad (3)$$

where \mathbf{N} is the pixel noise matrix, which is a diagonal matrix as the pixel errors are treated as statistically uncorrelated. The inverse of the covariance matrix $\mathbf{A}^T \mathbf{N}^{-1} \mathbf{A}$ must exist. A small prior is added at the level of machine precision to ensure the matrix remains well conditioned.

The residual image after subtraction of the background (hereafter difference image) is then simply given in pixel coordinates by

$$D(x, y) = S(x, y) - \left(\sum_i A_i c_i \right) (x, y) \quad (4)$$

3.1.2. Kernel Types

We use four different kernel bases,

1. Sum of Gaussians basis: Gaussian functions multiplied by 2-dimensional polynomials

$$k_i(u, v) = e^{-(u^2+v^2)/2\sigma_n^2} u^p v^q \quad (5)$$

¹⁴ <https://github.com/rotsehub/ImageDiff>

TABLE 2
 χ^2 AND R VALUES OF DIFFERENCING USING DIFFERENT KERNELS FOR ROTSE FIELD RQA0137+1547 SHOWN IN FIG. 1.

Kernel Type	χ^2/dof	R value	Pull
Gaussian sum	0.82	0.97	$\mathcal{N}(-0.01, 0.91)$
Gauss Hermite	0.82	0.97	$\mathcal{N}(-0.01, 0.90)$
Delta Function	0.81	0.97	$\mathcal{N}(-0.01, 0.90)$
EMPCA	0.85	0.93	$\mathcal{N}(0.03, 0.94)$

where i runs over all permutation of n, p, q . The polynomial order expansion used is $0 \leq p + q \leq O_n$. The default choices for 3 Gaussians are $\sigma = [0.7, 1.5, 3.]$ with $O_n = [4, 3, 2]$. The resulting total number of kernels = $\sum_n (O_n + 1) \times (O_n + 2) / 2 = 31$.

2. Gauss Hermite polynomial basis: A Gaussian core is multiplied by Hermite polynomials giving

$$k_i(u, v) = e^{-(u^2+v^2)/2\sigma^2} H_m(u)H_n(v) \quad (6)$$

where $H_n(x) = (-1)^n e^{x^2} \frac{d^n}{dx^n} e^{-x^2}$ is the n^{th} order Hermite polynomial. An obvious merit of using the Gauss-Hermite kernels over symmetric Gaussian kernels is that the former can model asymmetry because of the odd-even nature of the Hermite polynomials. An asymmetric PSF can occur for many different reasons such as atmospheric conditions.

3. Delta function basis: This kernel constitutes only delta functions

$$k_{i,j}(u, v) = \delta(u - i)\delta(v - j) \quad (7)$$

An 11×11 pixel size kernel has 121 orthonormal, single pixel bases. The benefit of the delta function is that it is shape independent, so there is no parameter to tune. However, this may need regularization to ascertain well conditioning of the model to prevent from overfitting. See Becker et al. (2012) for an application of delta function kernels.

4. Principal Component Analysis basis: We have also adopted a principal component analysis (PCA) based image differencing. PCA is a technique of reducing data dimensionality without losing any significant feature of the data. The principal components are the eigenvectors of the covariance of the dataset. They are sorted by the eigenvalues in descending order, i.e., along the component with the highest eigenvalue (first component), the variance is maximized. From the kernel-convolved templates using one of the kernels above, we construct an orthogonal eigen-basis using PCA. So in this case, the basis set is transformed from image space to PCA space. We use the `empca` package (Bailey (2012)) to compute the PCA using the expectation maximization (EM) method.

The top panel of Fig. 1 shows a high S/N template image, a later survey image and the output difference image for a subimage of ROTSE SN field rqa0137 + 1547. The bottom panel shows a slice of the galaxy profile, the model PSF using the sum of Gaussian kernels and the residual from the subtraction. The right most plot shows the Pull distribution for the residuals in normal form (\mathcal{N}) defined

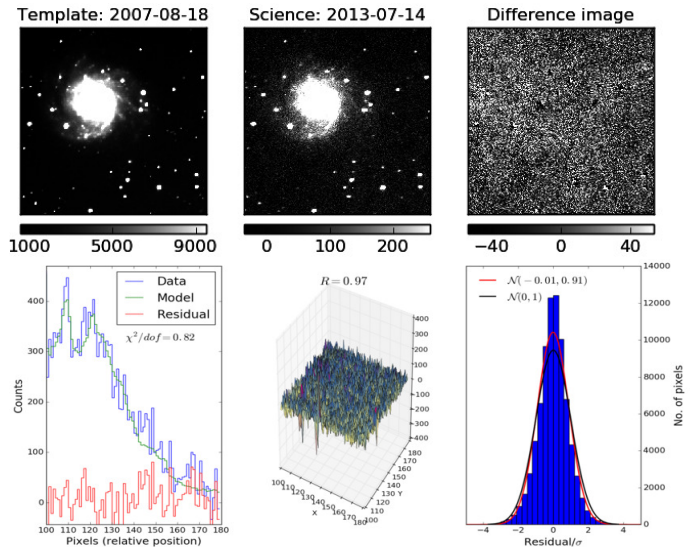


FIG. 1.— Top: A high S/N template subimage (left) and a survey subimage (middle) of the ROTSE IIb field rqa0137 + 1547, and the difference image using `ImageDiff` (right). Bottom: A slice from the center of the subimage showing the galaxy *M74* profile, the fit model and the residual (left); same residual in 2D shown in 80×80 pixels for clarity (middle), where R is the measure of the fraction of observation variance preserved in the difference image; pull distribution showing a Gaussian fit (red) yielding residual $\mathcal{N}(-0.01, 0.91)$ and the theoretical zero mean, unit variance standard normal distribution (black) in the right panel. The pull is close to standard normal distribution.

as

$$Pull = \sum_i \frac{data_i - model_i}{\sigma_i} \quad (8)$$

where i runs over all the pixels in the subimage. A performance summary of the image differencing algorithm using different kernel types on the same field survey image is shown in the Table 2.

3.1.3. Performance of Image Differencing

We monitor the performance of the differencing algorithm for both the spatial and temporal PSF variation in the following two ways. We simulate the PSF in order to establish the proper performance of the template subtraction, and we consider lightcurve properties to comment on efficiency and stability of source photometry. We consider the former using a PSF model profile with a Gaussian core and a wing component, allowing ellipticity variation from Bolton & Schlegel (2010):

$$I(x, y) = \frac{(1-b)}{\sqrt{2\pi}\sigma} e^{[-\frac{r^2}{2\sigma^2}]} + \frac{be^{(-r/r_0)}}{2\pi r r_0} \quad (9)$$

$$r_{ell} = \sqrt{qx^2 + y^2/q} \quad (10)$$

where b controls the wing contribution, r is the radial offset from the PSF center, r_0 is the characteristic size of the wing, q is the ellipticity and x & y are related to CCD coordinates by rotation/translation. Monte Carlo (MC) simulation is performed by injecting objects of random magnitudes at random locations within a subimage of a ROTSE survey image. To disallow tight blending of the injected source with the point data sources in the image, a `scikit` (Pedregosa et al. (2012)) $k-d$ tree query is performed taking a radius of 1 FWHM of the PSFs of the data image, derived by `sExtractor` (Bertin

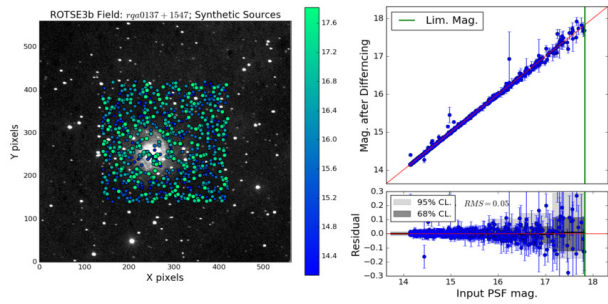


FIG. 2.— Left: 1000 simulated sources superimposed on a data image. Points show injected sources but do not represent the true PSF shape of the simulated objects. Right: Performance of `ImageDiff`. Overall residual mean is 0 yielding no bias, RMS ~ 0.05 magnitude; although close to the limiting magnitude, RMS ~ 0.1 mag. Pull distribution is $\sim \mathcal{N}(0.1, 0.94)$

& Arnouts 1996). For the injected sources, the image subtraction is performed iteratively one by one and the final photometry is performed on the difference image. The extracted magnitudes are compared with the input magnitudes. An example simulation for the ROTSE field *rqa0137 + 1546* is shown in Fig. 2. The RMS of the photometry residuals is at the 0.05 magnitude level, and a pull distribution shows normal $\sim \mathcal{N}(0.1, 0.94)$ distribution.

In most of the SNe analysed, the new image subtraction yields 10-20% more detections, and the scatter of the residuals also is remarkably narrower. The top panel of Fig. 3 shows an example of image differencing of an epoch of SN 2004gk using the new image subtraction software. The SN is clearly observed on the residual image on the right. The bottom panel shows the lightcurve of SN2004gk obtained using the old and new image subtraction. Each light curve is fitted with Gaussian Process (GP) regression using `scikit`. The rightmost plot shows the residuals of new and old light curves obtained after subtracting the GP best fit models. It is observed that the new image differencing not only has higher detection efficiency but also has over 3.5 times improvement in the residuals scatter. The pull distributions are found to be $\mathcal{N}(0.01, 1.03)$ for the new and $\mathcal{N}(0.39, 2.82)$ for the old method; suggesting no significant bias due to the new method. The typical pulls on the other SN light curves obtained with `ImageDiff` also follow within 10% of a standard normal distribution $\mathcal{N}(0, 1)$.

3.1.4. Photometric Calibration

ROTSE magnitudes are calibrated to magnitudes from the APASS¹⁵ DR9 catalog. These ROTSE magnitudes are corrected for extinction modeled from Schlafly & Finkbeiner (2011). Note that the ROTSE CCD response is significantly different than the *V* band filter response function. To establish a concrete and accurate calibration for the rapidly evolving Spectral Energy Distribution (SED) of SNe IIP, we quantify any potential offset associated with the calibration of ROTSE flux with the *V* band flux of the field stars. We perform Monte Carlo simulations of blackbody continuum spectra of varying temperature 2 kK- 17 kK, randomly normalized to *V* band magnitude in the range 12-18. The selection of

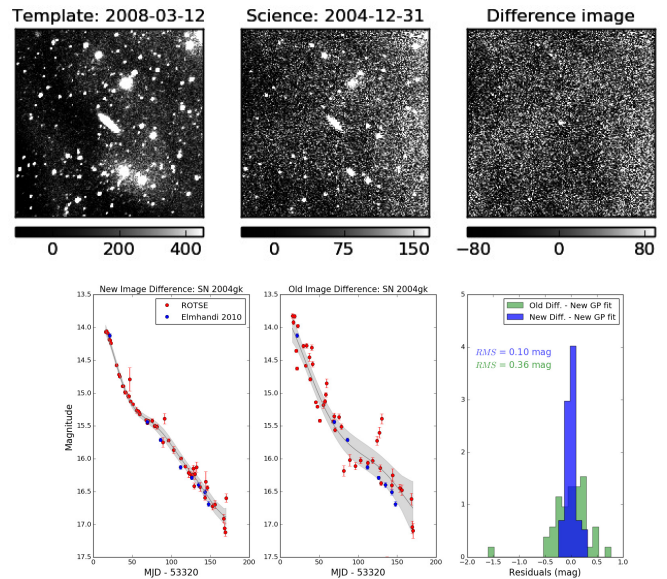


FIG. 3.— Top: Image subtraction of a 280×280 pixel subimage of ROTSE tss1246+1249 field: a high S/N template image (left) obtained with stacking 30 past images, a survey image with potential SN at the center (middle) and the difference image from `ImageDiff` using the sum of Gaussian kernel convolution of template image. SN 2004gk is clearly visible at the center of the difference image. Bottom: Photometric performance using new and old image differencing methods for SN 2004gk. The reduced data points are normalized to Elmhamdi et al. (2011) *V* band magnitude (shown in blue points), on MJD 53389.0 for training the eye. The solid line is a Gaussian Process regression fit, with the filled region being the 95% confidence posterior prediction. The rightmost panel shows the residuals of old (green) and new (blue) light curves after subtracting the respective best fits. The rms scatter for the green and blue histograms are respectively 0.36 and 0.10 mag, and the pulls on the new image differencing yield a dispersion of 1.03, which is substantially improved compared to the old differencing, where the pull yields a dispersion of 2.82.

temperature range (Section 5.3) and magnitude range agrees with the observed SN IIP temperatures and magnitudes for epochs similar to those in the sample. The blackbody spectra are convolved with the ROTSE response function and the *V* band filter response function, and magnitudes are estimated. The left plot of Fig. 4 shows the comparison of the simulated magnitudes for the ROTSE and *V* band. It is clear from the scatter that there is need for correction in both directions. To address these offsets, we use an exponentially growing function of temperature (*T*)

$$m_{ROTSE,V} - V = a + b(1 - e^{cT}) \equiv corr \quad (11)$$

where $m_{ROTSE,V}$ is the magnitude obtained from calibrating to *V* data before correction. The final calibrated magnitude is then $m_{ROTSE,V} - corr$. Best fit model parameters obtained using the simulation of 100 random blackbody spectra yield $a = -9.46 \pm 0.11$; $b = 9.52 \pm 0.11$ and $c = (8.06 \pm 0.048) \times 10^{-4}$. The state before correction, the correction model and magnitudes after applying the correction for the 100 Monte Carlo sample are shown in the middle and the right plot of Fig. 4. The RMS in the residuals is about 0.01 mag and no fundamental bias is observed from the correction. The residual RMS is much smaller than the typical statistical uncertainty of the obtained ROTSE magnitudes and is propagated as uncorrelated systematic uncertainty in the final

¹⁵ <https://www.aavso.org/apass>

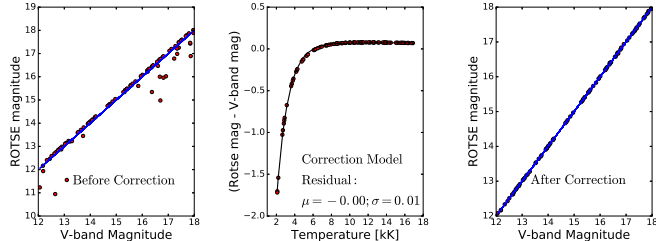


FIG. 4.— Correction of systematic effects of calibrating ROTSE magnitudes to catalog V band data. Shown are the offsets in scatter plot for 100 Monte Carlo blackbody spectra spanning 2000K to 17000K temperature, randomly normalized to V band mag range 12-18 (left), offsets varying with temperature and the correction model given by Eq. 11(middle) and offsets after applying correction (right).

photometry. As broadband observations are not available for the events in the sample at all epochs; and we are explicitly measuring and modeling temperature evolution in Section 5, we used a temperature dependent correction model. A color dependent correction would require broadband observations at the photometric epochs. When compared with the available V band data of several IIP SNe in the sample, the corrected photometric measurements during the plateau phase are obtained to be statistically consistent.

3.2. Spectroscopy

HET data are reduced using standard spectroscopic techniques as described in (Silverman et al. (2012); Dhungana et al. (2016)). Other spectra are obtained in the fully reduced form from the literature or from databases. All the spectra are converted to SN rest frame and corrected for reddening using the Fitzpatrick (1999) model.

3.3. Extinction, redshift and explosion epochs

Table 1 provides our adopted extinction, redshift and the explosion epochs for each event in our sample. We refer to the literature for respective measurements. When no extinction is available for the host, we adopt MW extinction only using Schlafly & Finkbeiner (2011). When the explosion epochs are not available, we adopt the arithmetic mean of the first detection and latest non detection in the ROTSE photometry or such reported in the literature, whichever provides the best constraint. For our sample, explosion epochs have uncertainty of 0.3 to 4 days. The redshifts are taken from the literature or the galactic redshift from the NED¹⁶ database unless otherwise noted.

3.4. K -Correction

Since we do not have color information from broadband photometry for all the events in our sample, we perform a spectrophotometric approach to obtain the K -correction for events with $z > 0.01$. First, to determine the K correction for each event, the spectroscopic data of all

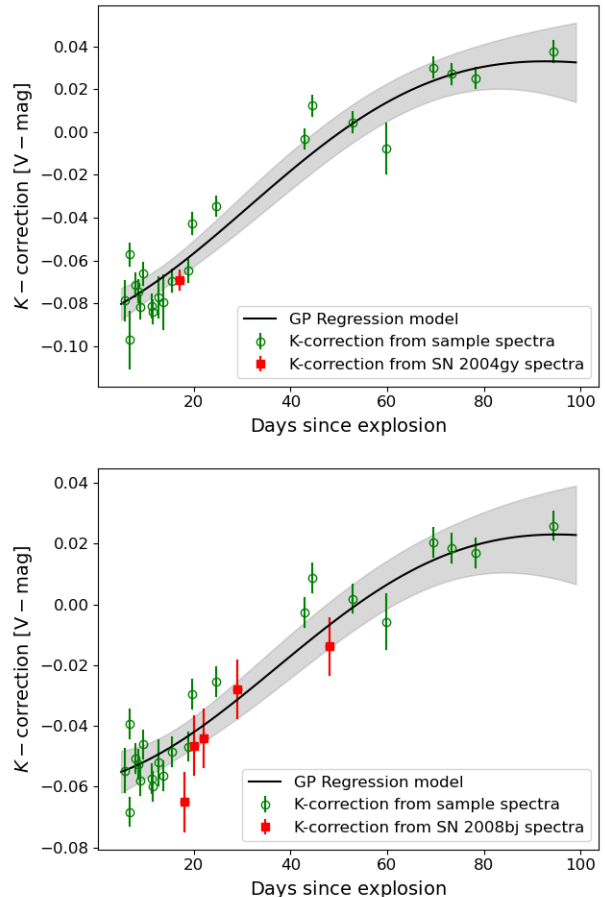


FIG. 5.— Top: K -corrections derived spectroscopically from the $z < 0.01$ SNe sample (green circles) and the SN2004gy spectrum (red squares) for $z = 0.0269$, corresponding to SN 2004gy. The solid line is the best fit GP model and the shaded region represents the 68% confidence region for the posterior. Bottom: The same as top for $z = 0.019$, corresponding to SN 2008bj.

the nearby SNe ($z < 0.01$) samples during the plateau phase are redshifted by the value for the SN considered and both the observer frame and the SN rest frame magnitudes are taken by applying the V band filter. The difference of the rest frame magnitudes from the observer frame gives the K -correction for the respective spectroscopic epochs. Once the K corrections are obtained from the sample at the spectroscopic epochs, they are also evaluated for the spectra of the SN for which the K -correction is to be determined. A temporal Gaussian Process (GP) regression is performed on the obtained K -correction values to make a prediction of K -correction for the desired photometric epochs of each SN with $z > 0.01$. An example GP regression fit and the 68% confidence level posterior prediction is shown in Fig. 5 for SN 2004gy (top) and SN 2008bj (bottom).

The final, fully reduced lightcurves for the ROTSE IIP SN sample, after calibration to APASS V magnitude and SED, and corrected for extinction and K -correction (for $z > 0.01$) are shown in Fig. 6.

4. EXPANDING PHOTOSPHERE METHOD AND OBSERVABLES

With the advent of more sensitive, deeper surveys, SNe IIP discovery is increasing. While competitive samples

¹⁶ <https://ned.ipac.caltech.edu/>

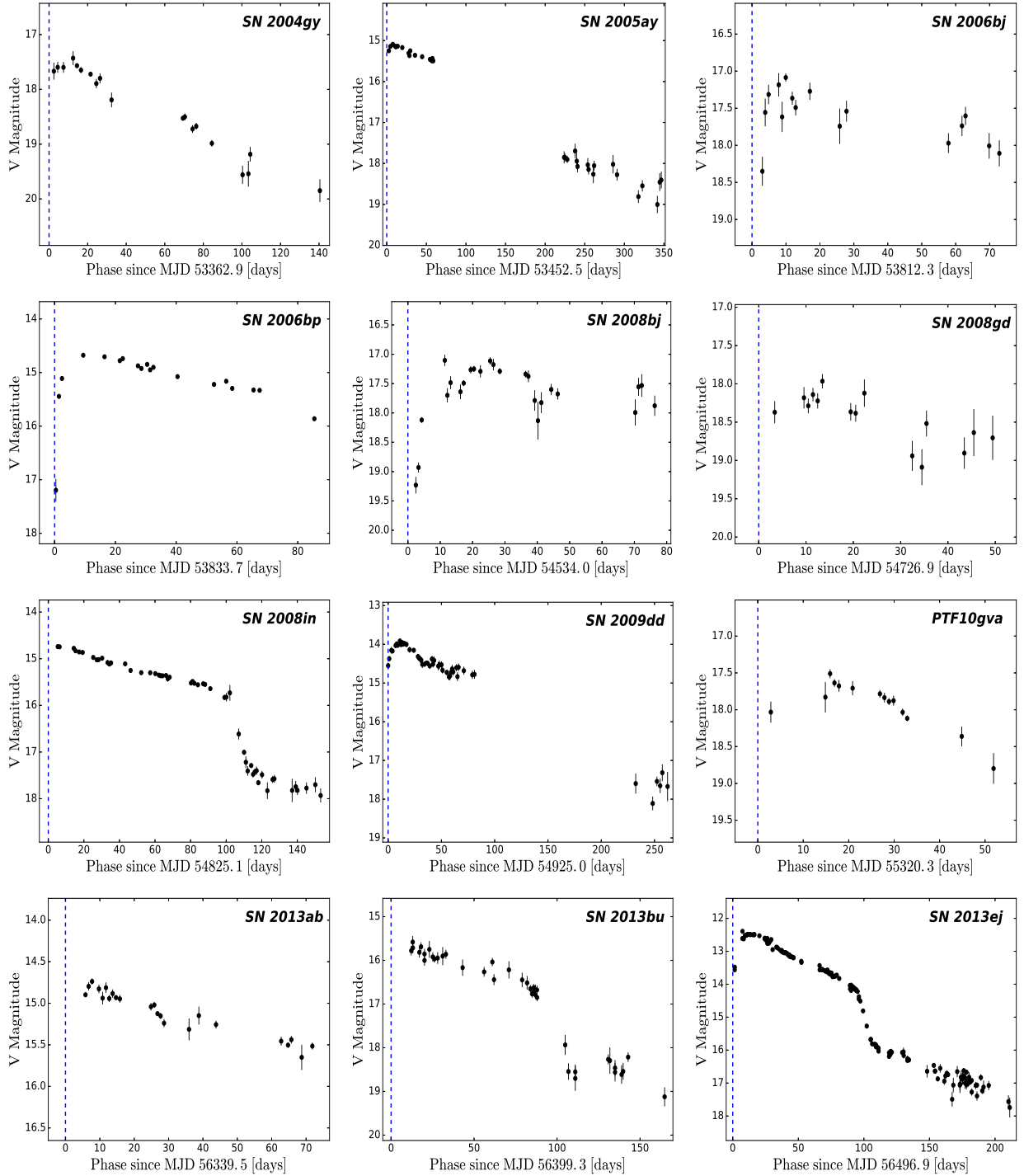


FIG. 6.— Lightcurves of SNe in the ROTSE IIP sample after final photometric reduction and calibration. The ROTSE magnitudes are calibrated to APASS V band, followed by the SED correction using Eq. 11 and the extinction correction. SNe with $z > 0.01$ also include an additional K -correction. Blue dashed lines on each plot represents the adopted explosion epoch for the respective event.

to perform precise cosmological study at the higher redshifts are still accumulating, improvements in calibration for distance estimates have been explored using both photometry and spectroscopy in the lower redshift domain. We utilize the Expanding Photosphere Method (EPM) to estimate distances of our SNe IIP sample. We follow the prescription of Dhungana et al. (2016); Dhungana (2018) to describe the fundamental EPM equation, given by

$$t = D \times \left(\frac{\theta}{v_{\text{phot}}} \right) + t_0, \quad (12)$$

where t represents the observing time, D is the distance to the SN, $\theta = 2R/D$ is the angular size of the photosphere at t , v_{phot} is the expansion velocity of the photosphere at t , and t_0 is the moment of the shock-breakout.

Assuming isotropic radiation from a blackbody, the observed flux can be written as

$$f_{\lambda}^{\text{obs}} = \theta^2 \pi B_{\lambda}(T) 10^{-0.4A_{\lambda}} \quad (13)$$

where $B_{\lambda}(T)$ is the Planck function for the blackbody of effective temperature T . A is the galactic extinction for the observed photometric band. The subscript λ should be taken as an index for the observed photometric bands. Unlike a perfect blackbody, where the thermal photons emerge from the photosphere, the surface of last scattering (e.g., Jones et al. (2009); Bose & Kumar (2014)), SNe IIP photons are generated from the deeper atmosphere. Therefore, the parameter θ in Eq. 12 corresponds to the thermalization layer while v_{phot} in Eq. 12 corresponds to the photosphere (optical depth, $\tau = 2/3$) and the atmosphere is considered gray (e.g., Jones et al. (2009); Eastman, Schmidt & Kirshner (1996)). A scaling factor ζ , also termed the dilution factor or distance correction factor, is introduced as ratio of the radius of the thermalization layer to that of the photosphere.

$$\zeta = \frac{R_{\text{therm}}}{R_{\text{phot}}} \quad (14)$$

Commonly, ζ is treated as a wavelength independent parameter in the optical and infra-red regime as described by Eastman, Schmidt & Kirshner (1996), who also show that it is a monotonic function of T for several weeks after the explosion. Thus, to exploit EPM on SNe, care should be taken to select the measurement epochs when the wavelength dependence is not very significant. Complex computation of a realistic model atmosphere is required to accurately estimate ζ , and is beyond the scope of this paper. We employ the commonly used prescription of Dessart & Hillier (2005), and include ζ_{λ} in Eq. 13.

$$f_{\lambda}^{\text{obs}} = \zeta_{\lambda}(T)^2 \theta^2 \pi B_{\lambda}(T) 10^{-0.4A_{\lambda}} \quad (15)$$

Ideally, one could consider full extinction-corrected bolometric flux by integrating over all the wavelengths. With the bolometric flux, θ can be obtained with

$$\theta = \frac{1}{\zeta(T)} \sqrt{\frac{f_{\text{bol}}}{\sigma T_{\text{eff}}^4}}, \quad (16)$$

where σ is the Stefan–Boltzmann constant. However, direct measurements of bolometric flux are not obtained in practice. Photometry is performed using specific pass

bands. Thus, the filter response function is always convolved with the native flux from a SN, giving its magnitude in that wave band. Many SNe in the ROTSE IIP sample lack observations to yield or calibrate to the full bolometric flux. Therefore, we derive the effective blackbody flux by convolving with the filter response function $R_{\lambda}(\lambda)$. i.e.,

$$b_{\lambda}(T) = \int_0^{\infty} R_{\lambda}(\lambda') \pi B(\lambda', T) d\lambda' \quad (17)$$

Therefore, with the observed flux in a given pass band λ and for the given value of $\zeta_{\lambda}(T)$, θ can be obtained using

$$f_{\lambda}^{\text{obs}} = \zeta_{\lambda}(T)^2 \theta^2 b_{\lambda}(T) 10^{-0.4A_{\lambda}} \quad (18)$$

The observed fluxes here should be treated as the K -corrected flux, whereas the parameters ζ_{λ} and b_{λ} are in the SN rest frame. K -correction accounts for the $(1+z)$ factors that would appear in the equations for high redshift SNe. Thus the derived distance will be the luminosity distance and not the angular diameter distance. We refer readers to Gall et al. (2016) and references therein for further discussion. The distance can be estimated using Eq. 12 by determining v_{phot} and T , which can be directly obtained from observations. Then, both the parameters D and t_0 can be simultaneously obtained by minimizing the χ^2 using

$$\chi^2 = \sum_j \frac{[\frac{\theta_j}{v_{\text{phot}_j}} - \frac{(t_j - t_0)}{D}]^2}{\sigma_j^2} \quad (19)$$

where σ_j is the uncertainty on $\theta_j/v_{\text{phot}_j}$.

5. SNE IIP PROPERTIES

The EPM distance estimation from Eq. 19 now requires for each event a sample of v_{phot} and θ measurements. While v_{phot} at any epoch can be estimated from the line profiles in a spectrum, θ is obtained through temperature estimation and comparison with the concurrently observed photometric flux using Eq. 15. In practice, however, both the spectroscopic and photometric measurements do not occur concurrently. Based on the available data, we will establish below the interpolation/extrapolation models to estimate the parameters at the desired epochs.

5.1. Explosion Epoch

Whenever available, the moment of explosion (t_0) for each of the IIP SNe sample is adopted from the literature as noted in Section 3.3. When no estimate is available, we take t_0 to be the midpoint of the first of the ROTSE or a publicly available photometric detection, and the most recent pre-discovery non-detection epoch in the ROTSE data. We propagate the difference of t_0 and the pre-discovery epoch to the systematic uncertainty in t_0 . Both the adopted explosion epoch and the respective uncertainty are given in Table 1.

5.2. Photospheric Velocity

As the SN IIP ejecta exhibit an extensive H-envelope during early times, the photospheric velocities are generally estimated directly from the weak line signatures such as those of Fe II lines. While in the plateau phase, the

absorption minima of the P Cygni profiles of Fe II $\lambda 4924$, $\lambda 5018$ and $\lambda 5169$ have been used as the best estimators of the photospheric velocity (e.g Leonard et al. (2002); Dessart & Hillier (2005); Nugent et al. (2006)), in the earlier epochs these lines cannot be observed. When observed, we strictly use Fe II $\lambda 5169$ velocity measurements for the v_{phot} . When Fe II $\lambda 5169$ is not observed at early times, we use He II $\lambda 5876$ line. On rare occasions, when He II also are not observed, we use correlations of H Balmer line velocity with Fe II line velocity from Faran et al. (2014) to obtain an effective v_{phot} .

5.2.1. Measurement

A convenient way to estimate the position of the line minimum is to perform a Gaussian fit of the absorption profile. Accurate measurements are complicated by typically blended features and continuum subtraction. We perform a 1D Gaussian mixture modeling (GMM) of a segment of the spectrum around each line of interest. We define a signal region considering the whole line profile. We consider a few 100s of Angstroms on both sides of the signal region as the side bins and a continuum is estimated by performing a spline fit on the side bins. GMM is performed iteratively on the continuum subtracted absorption profile. The best fit GMM model gives the optimum number of the Gaussian components as the maximum likelihood fit of this absorption profile. We measure the Bayesian Information Criterion (BIC) and Akaike Information Criterion (AIC) for each model as we increase the number of components for each iteration. The model that yields the minimum BIC from the GMM fit is chosen to be the best model. We monitor AIC also to ensure that it does not severely contradict with the best model from the minimum BIC value. The position of the component aligned with the line of interest will give the best fit value and the uncertainty of the photospheric velocity. An example involving this process of estimating line velocity for the H β line taking a spectrum for SN 2004gy from Jan. 10, 2005 is shown in Fig. 7. The top left panel shows the estimation of the continuum obtained from the spline fit performed on the side bins around the signal region of 4500 - 5000 Å. On the top right is shown the normalized residuals on the absorption profile after subtracting the continuum. GMM is performed iteratively by varying the number of components from 0–9. The bottom right panel shows the corresponding BIC and AIC values for each mixture model. The best fit model with the minimum BIC has six Gaussian components and the corresponding model and the Gaussian components are shown on the top right panel. The line velocity is obtained from the minimum of the Gaussian component corresponding to H β and is estimated to be 10760 ± 176 km/s, shown on the bottom left panel.

5.2.2. Extrapolation Model

Once the ionic velocities are measured directly from the GMM on the observed spectra, we want to interpolate/extrapolate these measurements to the photometric observation epochs. Previous studies such as Poznanski et al. (2010); Faran et al. (2014) have empirically modeled the temporal evolution of prominent ionic signatures such as from Fe II lines. While Fe II lines tend to track the photospheric velocity, these lines are generally unobserved during the first few weeks. We show below that

extrapolating such a model to early times shows a steeper decline than the velocities directly observed from He II lines.

We assemble the line velocities of three well sampled supernovae from the literature and observe the time series evolution of the v_{phot} . We first test an exponentially decaying model that appears to closely capture the v_{phot} evolution for each event during the epochs considered. Furthermore, when the epochs and v_{phot} of each SNe are calibrated relative to 50 day values, and the exponential model is fitted on the full distribution, we observe the RMS scatter to decrease significantly, yielding a reasonable χ^2/dof of 0.60 for the fit. We note that the choice of 50d has been commonly made in the literature and for SNe IIP, this is about midpoint of the typical plateau phase where the evolution is relatively smooth. We use an exponentially decaying model for the velocity evolution, given by

$$\frac{v_{\text{phot}}(t)}{v_{\text{phot}}(50)} = a + b \exp[-c \cdot (t/50)]. \quad (20)$$

The best fit parameters for the velocity evolution in Eq. 20 are estimated to be $a = 0.735 \pm 0.025$, $b = 2.650 \pm 0.064$; and $c = 2.327 \pm 0.589$. The left panel of Fig. 8 shows the time evolution of the v_{phot} for three SNe obtained from the GMM fit of the absorption profile of ions during the photospheric period. The middle left plot shows our best fit model after calibrating relative to 50 days. The middle right plot shows the residuals for different models after subtracting v_{phot} evolution best fit model shown in the middle left panel. Blue line is the residual for velocity model, obtained using Fe II only lines extrapolated in the earlier times, after subtracting best fit v_{phot} model. Also shown in red correspond to the residual for Fe II evolution model from Faran et al. (2014) extrapolated at early times, after subtracting the same best fit model. For comparison, all three models are anchored at $v_{\text{phot}}(50) = 4000$ km/s and the respective shaded region indicates the 68% confidence region. We see the Fe II only model yields a steeper velocity evolution than the v_{phot} model using He II lines at early times.

To estimate the v_{phot} for our IIP sample, we first measure line velocities directly from the obtained spectra of the respective SNe. We apply the v_{phot} evolution model Eq. 20 to obtain the $v_{\text{phot}}(50)$, and use it as anchor to sample the velocities at the desired photometric epochs. For events with multiple spectra, a weighted mean of $v_{\text{phot}}(50)$ is obtained and the v_{phot} at the photometric epochs are obtained anchoring the model Eq. 20 using this average $v_{\text{phot}}(50)$. We propagate the statistical error as uncorrelated systematic uncertainty from v_{phot} into the distance error budget for each SN. An example showing the directly estimated v_{phot} and the evolution model for the SN 2005ay is shown in the right most plot of Fig. 8. The blue points are the measured velocities for the labelled ions. The black dashed curves are the respective model pivoted at the measurement epoch, while the red dashed curve is the model anchored at the average $v_{\text{phot}}(50)$ measurement and red points are the velocity estimates at the photometric epochs of the SN. We perform the same procedure for all 12 events in our SNe IIP sample. We propagate the uncertainty on v_{phot} due

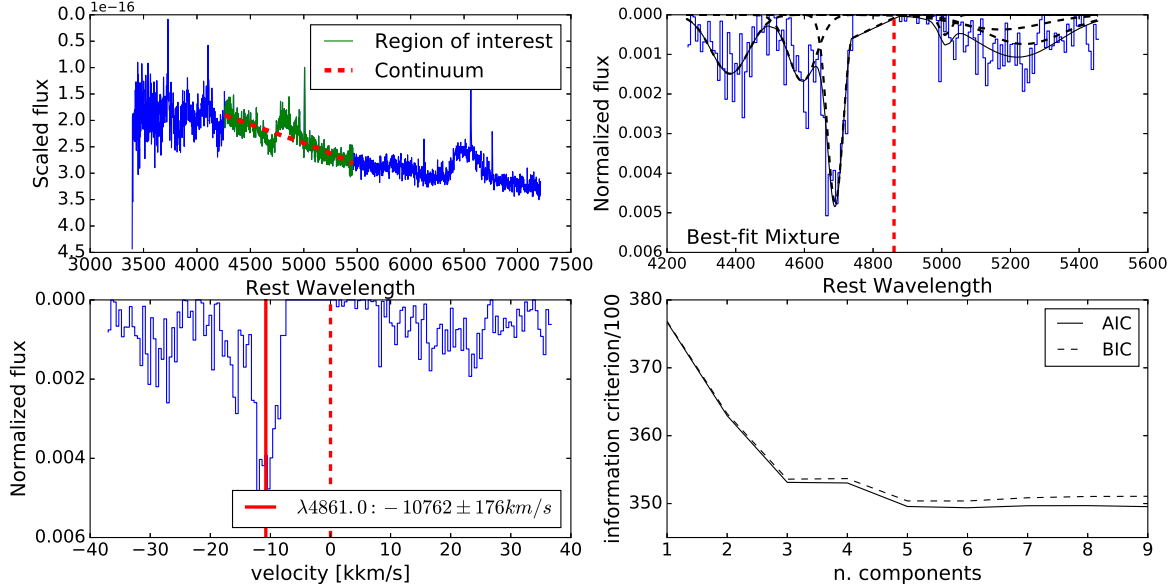


FIG. 7.— Estimation of the velocity of the $H\beta$ line using the GMM model. Top Left: A spectrum of SN 2004gy taken on Jan 10, 2005. The continuum is estimated using a spline fit on the side bins around the signal region of 4500 – 5000 Å. Top Right: The normalized residuals on the continuum subtracted absorption profile. The best fit mixture model is shown in solid black and the respective 6 Gaussian components are shown in dashed black lines. The dashed vertical line is the rest frame line position for $H\beta$. Bottom Left: Estimation of the line velocity from the best fit. The dashed vertical line indicates the rest frame position of $H\beta$ and the solid line shows the position of the absorption minimum obtained from the best fit. Bottom Right: BIC and AIC estimation for mixture model with multiple number of Gaussian components (n) performed iteratively for $n=0-9$. The best fit has minimum BIC and corresponds to $n=6$

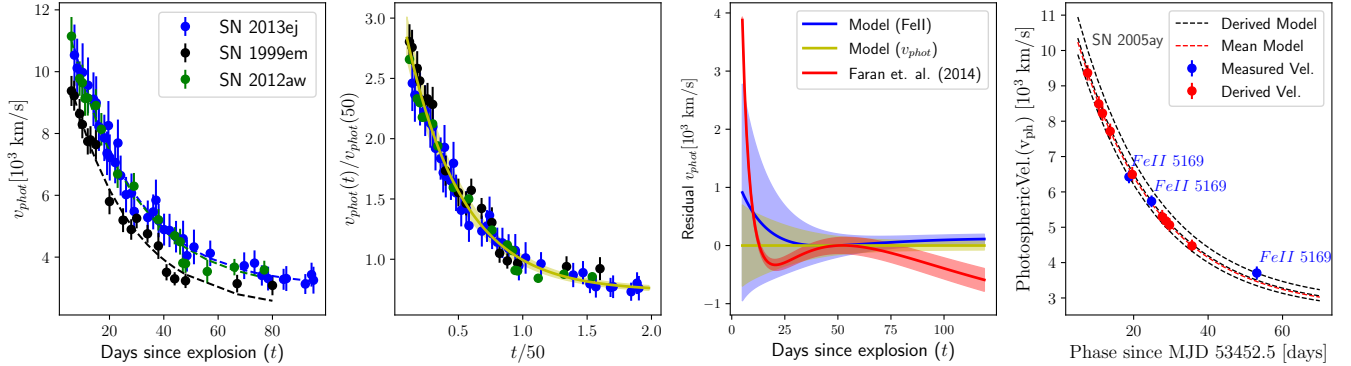


FIG. 8.— Left: Measured photometric velocities and the evolution for three well studied SNe IIP. Each velocity is derived from fitting relevant spectral lines using the GMM model from the spectra at corresponding epochs. The color-coded dashed lines represent the exponential decay law fits using Eq. 20 for the respective events. Middle Left: The global decay law fit after calibrating the epochs and v_{phot} relative to 50 day values for each of the SNe. The best fit model, shown with the solid line, has a $\chi^2/\text{dof} = 0.60$. Middle Right: The residual velocity evolution models after subtracting the best fit v_{phot} model shown in the middle left panel. The residual obtained for model obtained using Fe II lines alone is shown in blue and the red line is the residual obtained for the Fe II model evolution from Faran et al. (2014). All three are shown relative to an arbitrary pivot point of $v_{\text{phot}}(50) = 4000$ km/s. Right: Measured and derived v_{phot} models for SN 2005ay using the best fit model. The blue points are the labelled ion velocities measured directly from the spectra using GMM. The black dashed curves are the respective v_{phot} models calibrated to the three blue points. The red dashed curve is the model calibrated to the weighted mean velocity $v_{\text{phot}}(50)$ and red points are the derived estimates at the SN photometric epochs.

to the evolution model as a 100% correlated uncertainty across all 12 SNe in the sample.

5.3. Temperature

The parameter θ in Eq. 19 is obtained by comparing the observed flux from the SN with the effective blackbody flux after accounting for the dilution correction as shown in Eq. 15. To determine the effective blackbody flux, we would like to estimate the temperature from fitting the SED constructed from the *BVI* photometric measurements to a Planck function.

5.3.1. Measurement

For the events where *BVI* observations are available, we fit the measured SED to a Planck function directly and temperature is directly obtained as a fit parameter. For other events, to estimate the effective color or blackbody temperature, we take the spectra and spectrophotometrically determine the *BVI* fluxes. For this, each redshift corrected spectrum is unreddened for the galactic extinction by applying the reddening curve using the parametrization from Fitzpatrick (1999). The color extinction $E(B - V)$ is obtained for respective SNe from the literature, while Schlafly & Finkbeiner (2011) is used for the Milky-way extinction if no such information is available. After this, we derive a set of synthetic *BVI* magnitudes at the rest frame, and the resulting SED is fitted to a Planck function to estimate the effective temperature as before. For cases where the spectral coverage is not wide enough to synthesize the *BVI* fluxes, the corrected spectrum is fitted directly to the Planck function after masking the $H\alpha$ line and the telluric lines from the atmosphere when present.

5.3.2. Extrapolation Model

To estimate the temperature at the ROTSE photometric epochs, we first establish an analytic relation of the temperature evolution empirically using a sample of very well observed SNe IIP. As shown in the left panel of Fig. 9, an exponentially decaying model appears to accurately capture the temperature evolution for each event during the epochs considered. We pursue an approach to generate our temperature evolution model analogously to the velocity evolution model described in Section 5.2.2. We translate the epochs and temperatures of each SNe relative to 50 day values and perform an exponentially decaying model fit on all three SNe. We observe the RMS scatter to decrease significantly as shown in the middle panel of Fig. 9. The choice of 50 day epoch is consistent with the velocity evolution model. The exponential model for the temperature evolution is given by

$$\frac{T(t)}{T(50)} = a + b \exp[-c \cdot (t/50)] \quad (21)$$

The best fit model for the full sample yields $a = 0.908 \pm 0.012$, $b = 2.662 \pm 0.091$ and $c = 3.492 \pm 0.143$, as shown in Fig. 9, and yields a $\chi^2/dof = 1.04$. We also note that a power law model with decay index of -0.44 ± 0.01 also yields a reasonable estimate with a $\chi^2/dof = 1.6$. The adopted exponential model serves to reproduce the full temperature evolution if one temperature is measured at any epoch. The temperature estimated directly from the *BVI* fluxes is used to estimate $T(50)$ using Eq. 21.

Similar to the photospheric velocity evolution, for events with multiple spectra, the final temperature evolution is derived from the weighted mean $T(50)$ value. The estimated $T(50)$ is then used to anchor the model to desired photometric epochs. The evolving temperatures are sampled from this model at the ROTSE photometric epochs between +7d and +35d. The statistical uncertainty for each SN is propagated as an uncorrelated systematic uncertainty from the temperature evolution into the distance error budget. The measured temperatures, the extrapolation models and the respective final estimate at the ROTSE epochs for SN 2005ay are shown in the right panel of Fig. 9. For each SN in the sample, we propagate the extrapolation model uncertainty as a correlated systematic uncertainty from this common temperature evolution model in the final distance error estimates. Table 3 shows the derived +50 day values of the photospheric velocity and the effective temperature for all 12 SNe in our IIP sample.

6. DISTANCE MEASUREMENT

We have established the overall methodology and the various inputs that will go into our measurement of SN distance. The photometric measurements and their relationships with the EPM parameters are discussed in Section 4. The best fit distance for each SN is estimated by χ^2 minimization using Eq. 19. We next identify systematic effects that could impact our results and assess their magnitude on the final measurements. As we have modeled both the temperature and the photospheric velocity anchored at the 50 day estimate, in each case, there are two categories of systematic uncertainties that are propagated to the final distance estimation. One is the uncorrelated systematic uncertainty from the uncertainty on the respective 50 day value, while the other is the correlated systematic uncertainty from the modeling of those parameters at the photometric epochs of each SNe. Both of these uncertainties are propagated to the distance systematic uncertainty. The uncertainties in the galactic extinction (based on Schlafly & Finkbeiner (2011)) and the host extinction $E(B - V)$ are also transformed as uncorrelated systematic uncertainty in distance. The additional systematic uncertainty from the *K*-correction modeling is also propagated from the posterior estimate from the Gaussian Process regression. Finally, we also propagate the uncorrelated systematic uncertainties on the adopted t_0 , which are given in Table 1. Better constrained shock breakout times can significantly reduce the total uncertainty on the distance estimated with the EPM method. The fitted EPM distance and t_0 with the respective uncertainties from the fit are given in Table 3. All epochs including the fitted values of t_0 are relative to the adopted t_0 values in MJD from Table 1. We also note that the uncertainties on t_0 from the fit are consistent with the our adopted uncertainties in Table 1.

The systematic uncertainties in distance are also shown in Table 3; where the total uncorrelated systematic uncertainties in distance are calculated from the t_0 , $E(B - V)$, z uncertainties and the uncorrelated uncertainties from the velocity and temperature evolution models, all added in quadrature. The total correlated systematic uncertainty includes the contributions from the velocity and temperature evolution models, added in quadrature. Fig. 10 shows the best fit estimated distance measured

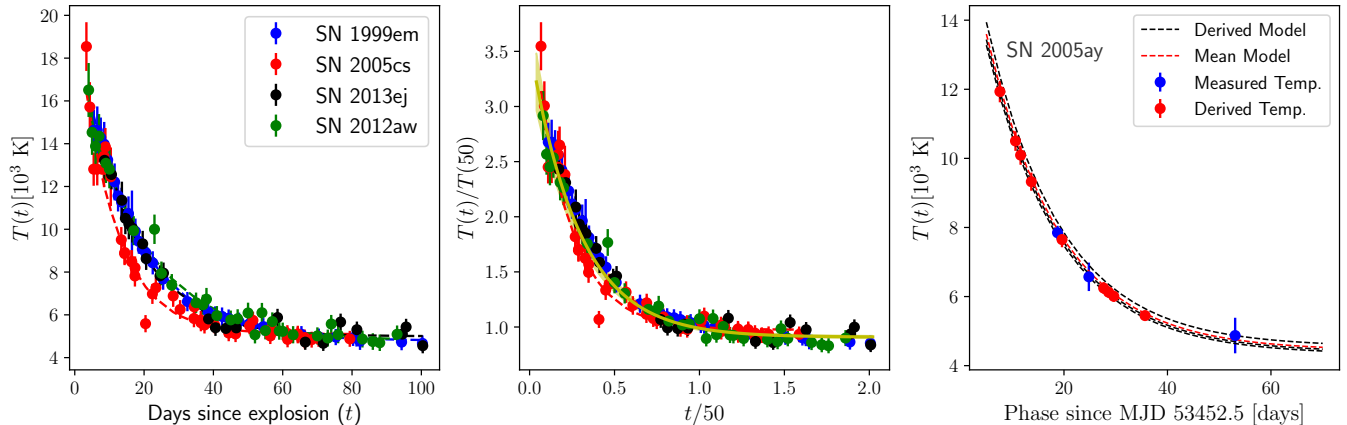


FIG. 9.— Left: Measured color temperature and the evolution model for four well studied SNe IIP. Each temperature is derived from fitting BVI fluxes to Planck function. The color-coded dashed lines represent the exponential decay law fits using Eq. 21 for the respective events. Middle: The global decay law fit after calibrating the epochs and temperature relative to 50 day values for each of the SNe. The best fit model, shown with the solid line, has a $\chi^2/dof = 1.04$. Right: Evolution of effective temperature for SN 2005ay. Blue points are the measured temperatures obtained from SED fit to Planck function. The dashed black lines are the model extrapolation anchored at each blue point, while the red dashed line is the effective model pivoted at the weighted average $T(50)$ value. Red points are the sampled model temperatures at the photometric epochs.

for each SN in our sample. In each of the SNe shown, the measured data points are given at the ROTSE photometric epochs and the solid lines represent the best fit solution using Eq. 19.

7. COSMOLOGICAL ANALYSIS

Using the luminosity distances derived above, we employ two methods to extract the Hubble constant (H_0) for the nearby universe. In one approach, we simulate the impact of peculiar velocities on a sample of 12 galaxies with distances according to the observed distribution and fit for H_0 . We also perform a Markov Chain Monte Carlo (MCMC) to obtain a parametric estimation of H_0 . In our analysis, we assume no sensitivity of our measurements to other cosmological parameters such as Ω_M and Ω_Λ . In each of these methods, we initially blind the fitted (H_0) parameter by translating with an unknown random additive scalar; which we un-blind at the end to obtain the final estimate.

7.1. Linear Fit of H_0

Peculiar velocities complicate the extraction of H_0 from the sample and they are substantial relative to recessional velocity for the lower redshift constituents of this survey. We attempt to mitigate this impact by simulating and fitting galaxies with peculiar velocities at the distances we have calculated. Recessional velocities are simulated according to

$$v = H_0 d \quad (22)$$

where H_0 is a parameter that can be specified and we note that this linear relationship holds for the redshift range considered here. We first simulate individual pseudo-experiments populated by SNe distributed according to the distances in Table 3. The recessional velocity for each galaxy in a pseudo-experiment is determined using Eq. 22.

Peculiar motion is modeled for each simulated galaxy by adding a random velocity component from a Gaussian distribution centered around 300 km s^{-1} , as is typically quoted in peculiar velocity studies (e.g. Kessler et

al. (2009), Davis et al. (2011), Johnson et al. (2014)). Each generated peculiar velocity is multiplied by a random value between -1 and 1 to account for the component along the line of sight. Errors in distance for the simulated galaxies are chosen to reflect the data sample uncertainties. Errors in velocity are set to 300 km s^{-1} . We split the analysis using a boundary at $cz_{CMB} = 3000 \text{ km s}^{-1}$, to distinguish whether peculiar velocity is large compared to the total velocity. Pseudo-experiments each including 7 galaxies with random distances of $5 \leq d \leq 30 \text{ Mpc}$ constitute the *local* sample. Pseudo-experiments each including 5 galaxies with random distances of $70 \leq d \leq 260 \text{ Mpc}$ constitute the *H-flow* sample. We then fit Eq. 22 to each pseudo-experiment, with H_0 as a free parameter forced to 0 at $z = 0$.

We test this fitting approach for potential bias on the extracted H_0 measurement. We generate 10,000 pseudo-experiments for both samples, repeating this process for input cosmologies of $50 \leq H_0 \leq 90 \text{ km s}^{-1} \text{ Mpc}^{-1}$ at $5 \text{ km s}^{-1} \text{ Mpc}^{-1}$ intervals. We calculate the measured value, H_0^{meas} , averaged over all pseudo-experiments of each ensemble with the specific input value, H_0^{true} . We apply a linear fit to H_0^{meas} vs. H_0^{true} , and obtain the values of slope to be 1.0011 ± 0.0007 and intercept of 0.0651 ± 0.0462 for the *local* sample. The corresponding fit parameters for the *H-flow* sample are 1.0012 ± 0.0007 and 0.0669 ± 0.0451 respectively. These fits yield a slope and offset close to 1.0 and 0.0, respectively, for both the *local* and *H-flow* samples, indicating small but non-negligible bias. Using the fit parameters, we construct calibration vectors with values for each instance of input H_0^{true} . The overall H_0^{meas} values for the “combined” sample are taken to be the weighted average of the *local* and *H-flow* sample measurements after the respective calibrations. A linear fit of H_0^{meas} vs. H_0^{true} for the *combined* sample results in a slope and offset of 0.9999 ± 0.0005 and 0.0005 ± 0.0371 , respectively, indicating an adequate mitigation. Differences between H_0^{meas} and H_0^{true} values, ΔH_0 , before and after calibration are

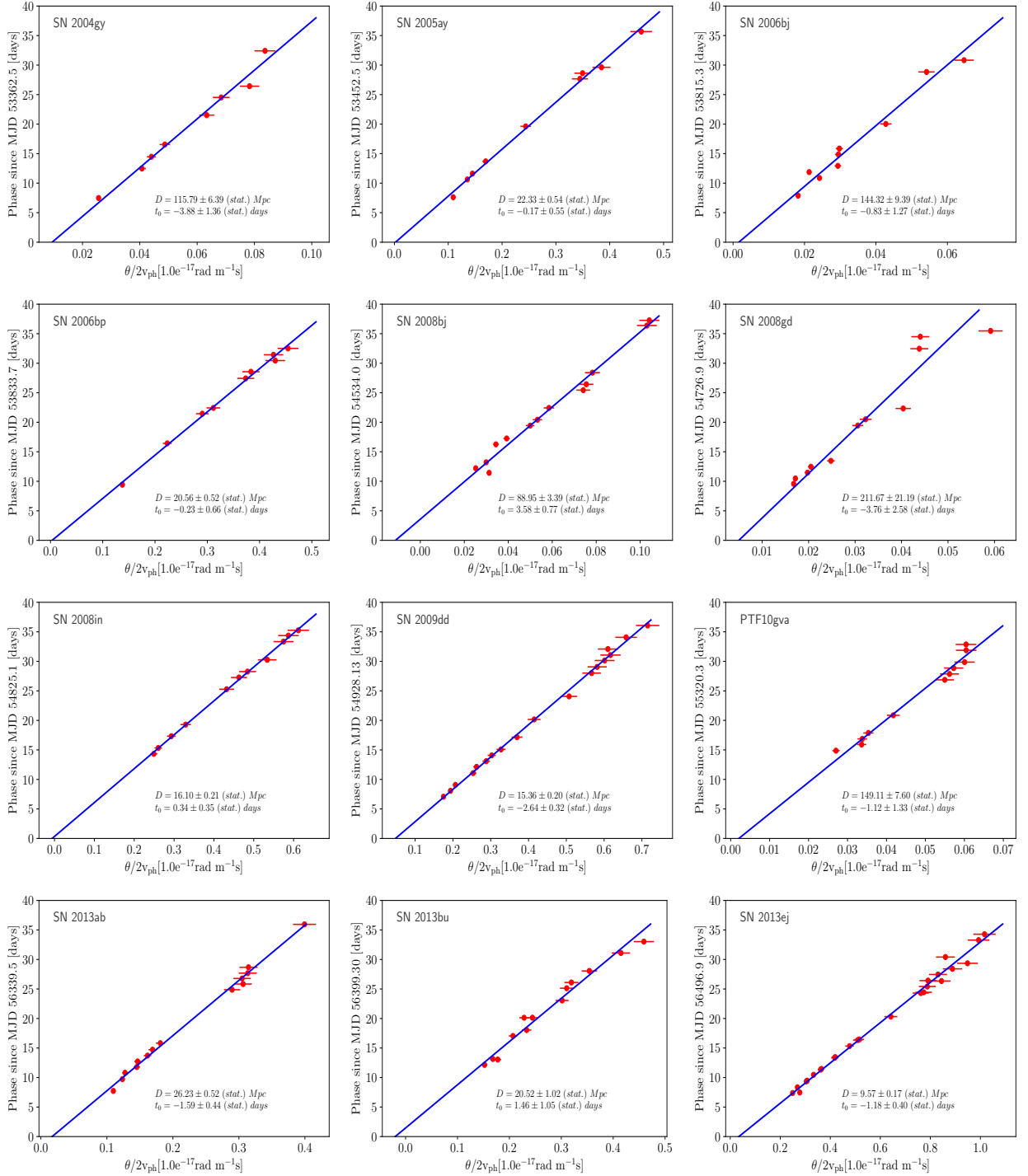


FIG. 10.— Distance estimates of the 12 ROTSE SNe IIP using the EPM method. In each case of the SNe shown, the measured data points are given at the ROTSE photometric epochs and the solid lines represent the best fit solution using Eq. 19.

TABLE 3
SUMMARY OF THE IIP PARAMETERS AND BEST FIT EPM DISTANCE AND t_0

SN	$v_{\text{phot}}(50)$	$T(50)$	$t_0(\text{days})$		Distance(d) (Mpc)			Median Distance from NED ^a	
	(10^3 km s^{-1})	(10^3 K)	Fit	(stat.)	Fit	(stat.)	(syst.)	(Mpc)	
							Total uncorr.	Total corr.	
SN2004gy	4.5 ± 0.2	5.2 ± 0.2	-3.88	1.36	115.78	6.39	12.04	6.06	NA
SN2005ay	3.9 ± 0.1	4.8 ± 0.1	-0.17	0.55	22.33	0.54	3.62	1.14	21.9
SN2006bj	4.4 ± 0.2	8.5 ± 0.3	-0.83	1.27	144.32	9.39	24.07	7.77	NA
SN2006bp	4.3 ± 0.1	4.6 ± 0.2	-0.23	0.66	20.56	0.52	1.76	1.07	17.5
SN2008bj	5.2 ± 0.2	6.2 ± 0.2	3.58	0.77	88.95	3.39	11.62	4.36	NA
SN2008gd	4.9 ± 0.2	6.4 ± 0.3	-3.76	2.58	211.67	21.19	32.17	10.96	NA
SN2008in	2.7 ± 0.1	5.5 ± 0.2	0.34	0.35	16.10	0.21	2.65	0.82	16.6
SN2009dd	3.7 ± 0.1	4.6 ± 0.2	-2.64	0.32	15.36	0.20	0.88	0.81	10.9
PTF10gva	5.2 ± 0.3	6.5 ± 0.2	-1.12	1.33	149.11	7.60	8.62	7.77	NA
SN2013ab	4.2 ± 0.2	4.9 ± 0.2	-1.59	0.44	26.23	0.51	2.96	1.36	23.5
SN2013bu	3.6 ± 0.1	3.7 ± 0.2	1.46	1.05	20.52	1.02	1.54	1.20	14.4(host)
SN2013ej	4.3 ± 0.1	5.5 ± 0.2	-1.18	0.40	9.57	0.17	0.29	0.49	9.5

The best fit distances and t_0 values for the 12 SNe IIP with respective statistical uncertainties from the EPM fits are given. Also shown are the total uncorrelated and correlated uncertainties for each of the distance measurements for the SN sample. In the rightmost column, median distances from NED catalog are also given for those SNe that have distances from redshift independent measurements. If no SN distance is available, host distances are given for reference whenever available.

^aRedshift independent distances from <https://ned.ipac.caltech.edu/>

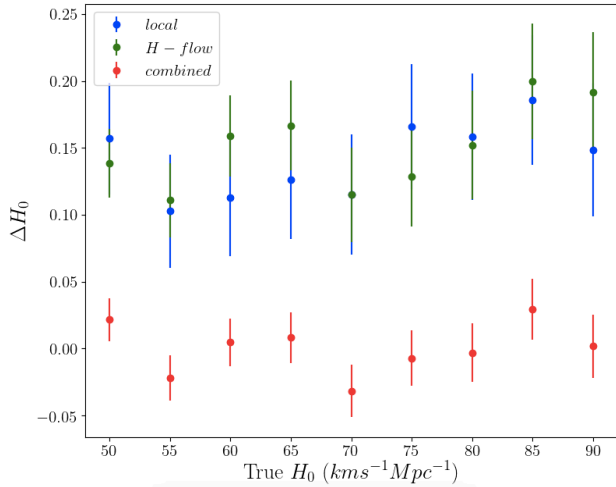


FIG. 11.— Residuals of average $H_0^{meas} - H_0^{true}$, ΔH_0 , for the simulated *local* and *H-flow* samples before calibration, and the *combined* sample after calibration. See text for the slopes and offsets.

shown in Fig. 11 for a range of tested H_0 values. The small estimated bias for each subsample and the efficacy of the corrections for the combined result, is independent of H_0 .

We apply the above procedure to the data, using the calibration vectors described above, for the *local* and *H-flow* samples, respectively. We obtain calibrated values of $H_0 = 67.4 \pm 11.8(stat) \text{ kms}^{-1} \text{ Mpc}^{-1}$ for the *local* sample and $H_0 = 75.6 \pm 5.1(stat) \text{ kms}^{-1} \text{ Mpc}^{-1}$ for the *H-flow* sample. The combined, weighted average yields a final value of $H_0 = 74.3 \pm 4.7(stat) \text{ kms}^{-1} \text{ Mpc}^{-1}$. The Hubble diagram from the fits of *local*, *H-flow* and the final estimates are shown on the top panel of Fig. 12. The blue and magenta dashed lines correspond to the fits to the *local* and *H-flow* samples and the red line correspond to the combined weighted estimate. The vertical error bars include the total uncorrelated uncertainty shown from Table 3 added in quadrature with the estimated distance uncertainty from 300 kms^{-1} fixed peculiar velocity; while the horizontal error bars represent that peculiar velocity uncertainty.

We assess an additional systematic uncertainty due to the correlated impact among the SNe from the velocity and temperature evolution model uncertainties. We add up the correlated errors from Table 3 for all SN distances and refit for H_0 . We repeat shifting the SN distances low by the correlated errors. The uncertainty on H_0 is calculated from the differences of these fits from the nominal H_0 value. This results in a modeling uncertainty of ${}^{+4.1}_{-3.7} \text{ kms}^{-1} \text{ Mpc}^{-1}$. A systematic uncertainty due to the assumption of typical peculiar velocity of 300 kms^{-1} was assessed by resimulating ensembles with $H_0 = 60, 70, 80 \text{ kms}^{-1} \text{ Mpc}^{-1}$ for distributions of peculiar velocity centered around 230 kms^{-1} and 370 kms^{-1} to estimate the lower and upper bounds of potential values of H_0 and peculiar velocity. This yielded an uncertainty of $\pm 0.3(sys) \text{ kms}^{-1} \text{ Mpc}^{-1}$.

7.2. Markov Chain Monte Carlo Sampling

We also perform a parametric estimation of a cosmological model using an MCMC simulation in a Bayesian

framework. For the given values of $(z_{CMB}, \Omega_M, \Omega_\Lambda)$, the luminosity distance (D_L) is given by

$$D_L = \frac{c}{H_0} \int_0^{z_{CMB}} \frac{dx}{\sqrt{\Omega_M(1+x)^3 + \Omega_\Lambda}} \quad (23)$$

We use the publicly available package EMCEE (Foreman-Mackey et al. (2013)), where the MCMC is performed to sample the posterior probability distribution obtained from the given likelihood function and the distribution of the priors. We expand the 1-D likelihood function discussed previously in (Poznanski et al. 2010; D’Andrea et al. 2010; de Jaeger et al. 2017) in 2 dimensional matrix form

$$\ln \mathcal{L} = -\frac{n}{2} \ln(\det(V)) - \frac{1}{2} \sum_{i=1}^n (D_i^{ms} - D_{Li}) V^{-1} (D_i^{ms} - D_{Li}) \quad (24)$$

where the sum is over ($n=12$) SNe in the sample. D_i^{ms} is the measured distance using EPM and D_{Li} is the luminosity distance using Eq. 23 for the i^{th} SN. The matrix V is given as

$$V = C + \sigma_{int}^2 I \quad (25)$$

where C is the covariance matrix and σ_{int} is the residual intrinsic uncertainty that includes any unaccounted uncertainty in the analysis. The diagonal terms of the covariance matrix C comprise the statistical uncertainties added in quadrature with the total uncorrelated systematic uncertainties from the Table 3, while the off-diagonal terms are computed by multiplying the total correlated systematic errors for respective SNe from Table 3. As in the linear fit analysis, we add in quadrature an uncorrelated uncertainty of 300 kms^{-1} in the diagonal terms to account for the contribution due to peculiar motion.

We consider a flat universe ($\Omega_M + \Omega_\Lambda = 1; \Omega_M = 0.3$) as our prior. The only free parameters are the Hubble parameter (H_0) and the intrinsic uncertainty σ_{int} . Now we are not only interested in the best fit values of these parameters, but also in their full maximum a *posteriori* probability density distribution. In the Bayesian framework, the joint posterior probability function for these parameters can be written as

$$p(H_0, \sigma_{int} | z_{CMB}, D_L, C, \Omega_M, \Omega_\Lambda) \propto p(H_0, \sigma_{int}) p(D_L | z_{CMB}, C, H_0, \sigma_{int}, \Omega_M, \Omega_\Lambda) \quad (26)$$

The function $p(D_L | z_{CMB}, C, H_0, \sigma_{int}, \Omega_M, \Omega_\Lambda)$ is the likelihood function \mathcal{L} given in Eq. 24; while for the prior distribution, $p(H_0, \sigma_{int})$, we chose flat priors given by

$$50 \text{ kms}^{-1} \text{ Mpc}^{-1} < H_0 < 150 \text{ kms}^{-1} \text{ Mpc}^{-1} \quad (27)$$

$$0 \text{ Mpc} < \sigma_{int} < 50 \text{ Mpc} \quad (28)$$

We first evaluate the best fit maximum likelihood estimation (MLE) values of H_0 and σ_{int} by minimizing the negative log of the likelihood in Eq. 24. Next, we initialize the MCMC chains by picking 500 random initial points as seeds by sampling a small 2-D Gaussian ball about the MLE of the parameters H_0 and σ_{int} . The MCMC is performed using the EMCEE framework for 500 steps for

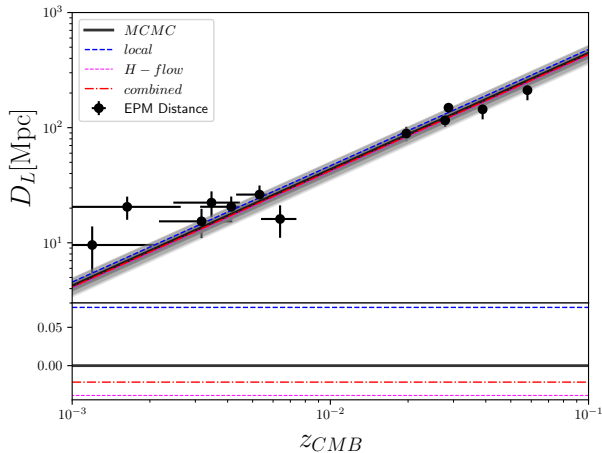


FIG. 12.— Top: Hubble diagram showing the posterior samples from MCMC in gray. The solid black line is the maximum likelihood estimate from the MCMC method. The black points are the measured luminosity distances using EPM. The blue and magenta dashed lines correspond to the linear fits to the *local* and *H-flow* samples and the red curve is the combined weighted estimate from the linear analysis. The horizontal error bars on the data points correspond to the assumed peculiar velocity of 300 km s^{-1} . Bottom: Residuals of the linear fits with respect to the best fit estimate from the MCMC analysis, shown as difference of log values

each walker; resulting in a joint posterior probability distribution $p(H_0, \sigma_{int})$. To avoid any systematic sampling bias from the choice of initialization, we discard the first 50 steps of each walker; after which the walkers begin to fully span the full posterior distribution.

The resulting Hubble diagram from the posterior samples are shown in the top panel of Fig. 12. The solid black line represents our best fit model from the MCMC analysis; and the gray lines represent the posterior samples from the MCMC runs. The black data points are the measured luminosity EPM distances for the SNe IIP sample. The vertical and horizontal error bars are described in Section 7.1. From the final marginalized 1-D posterior distributions, the Hubble parameter is estimated to be $72.9^{+5.7}_{-4.3} \text{ km s}^{-1} \text{ Mpc}^{-1}$ and the intrinsic scatter σ_{int} is estimated to be $0.3^{+0.42}_{-0.26} \text{ Mpc}$. The bottom panel of Fig. 12 shows the residuals of the obtained fits from the linear analysis in Section 7.1 relative to the best fit from the MCMC analysis shown in the difference of log values.

8. RESULTS AND DISCUSSION

Our aim has included development of a methodology for distance measurement of SNe IIP utilizing unfiltered CCD photometry and minimal color and spectroscopic data, and that would enable a sensitive probe of cosmic expansion. We had addressed this previously for SN 2013ej (Dhungana et al. 2016), which was far from the host nucleus and did not require an image differencing approach. However, analysis of a more representative survey of SNe IIP required a more general approach.

The new image differencing algorithm, `ImageDiff`, introduced in this paper was designed to obtain photometric measurements with high efficiency and consistency over a wide range of host environments. It also delivered photon-limited measurements unimpacted by artifacts and their attendant systematic uncertainties. The performance was assessed by injecting PSFs into an image with a full range of SN-nucleus displacements. This

showed that we could extract the simulated magnitudes precisely up to a limiting magnitude of ~ 18 and across the wide field of view. The performance study showed no significant bias in the photometric residuals as shown in Fig. 2. The new software demonstrated improved photometric detection efficiency up to 20%. By examining SN 2004gk, a typical SN with distance to host nucleus of $\sim 3''$, we are able to quantify the improvement over the prior image differencing code for ROTSE. The scatter in points around the known lightcurve is reduced by approximately 3 times to roughly 0.1 magnitude (Section 3.1.3) when compared to prior approaches used for the ROTSE SNe data reduction pipeline. The increased performance was particularly observed in the crowded fields and when the SN was closer to the host nucleus. We also note that for similar image sizes in most cases, the performance across several kernel bases were similar. These results are critical to what follows because the astrophysical and distance measurements produced in this study rely on minimizing photometric uncertainties overall.

In Dhungana et al. (2016), we demonstrated with SN 2013ej the ability to calibrate well the ROTSE unfiltered photometry to a pseudo-bolometric magnitude to facilitate the EPM extraction of distance. Such a method requires substantial color photometry spanning from the near ultraviolet to near infrared wavelengths at various epochs of the supernova. While that method yielded excellent photometry and an accurate distance measurement, we have attempted a different approach here that relied less on such extensive filtered photometry and spectroscopy by calibrating the ROTSE magnitude to the V-band magnitude and using color-based temperature estimates to improve the correction. We also established a V band calibration for the ROTSE unfiltered SNe lightcurves that were consistent with the observed V band SNe lightcurves from the literature. In the end, the correlation with an actual V-band magnitude, at 0.01 magnitudes, is of sufficient precision to obtain accurate distances while keeping the extensiveness of the required broadband photometry and spectroscopy to a minimum.

Utilizing filtered photometry and spectroscopy for several well measured SNe IIP, we saw that the velocity and temperature evolution exhibited similar behaviors. To quantify this evolution and provide a model from which these properties can be determined at any epoch, we established empirical calibrations for both properties' evolution using single epoch photometric and spectroscopic measurements (Section 5). The exponential decay behavior has been empirically observed in the literature of SNe IIP, but its physical origin appears to require further study. Modeling of the photospheric velocity evolution from the spectra indicates that the use of Fe II lines only, such as in Faran et al. (2014), does not accurately describe the early behavior when extrapolated. Using Fe II when observed and He II and H-alpha lines during early times makes the decline in velocity less steep in agreement with observed SNe (Section 5.2.2). This model also seems to improve the agreement with data sufficiently late in the plateau. Velocities measured for our IIP sample ranged from 2700 km s^{-1} to 5200 km s^{-1} at $t = 50\text{d}$. Remarkably, when normalizing values from other epochs to this value, the behavior for different events present a very precise exponential fall off with t ; supporting the ability to calibrate the evolution from measurement at

a single epoch. Interestingly, the temperature evolution appears to be well described by a similar exponential profile. The temperatures at 50d range widely from 3700 to 8500 K and yet the evolution lines up well, with the exception of SN 2005cs which is slightly steeper at early times and flatter than other SNe later. SN 2005cs has been very well studied in the literature and appears to be an outlier from the general population as an under-luminous SN. Nevertheless, the four SNe we examined yielded a good fit to Eq. 21.

Use of the EPM technique for distance measurements provided additional constraints on the supernova itself via the fit to t_0 . The precision yielded was as small as ± 8 hours. The fitted t_0 from the EPM were found consistent with our initially adopted values of t_0 . We were able to calculate the luminosity distance with limited unfiltered photometry and spectroscopy. Distances ranged from $9.57 \pm 0.17(\text{stat.}) \pm 0.29(\text{uncorr.}) \pm 0.49(\text{corr.})$ to $211.67 \pm 21.19(\text{stat.}) \pm 32.17(\text{uncorr.}) \pm 10.96(\text{corr.})$ Mpc. As shown in Table 3, these distance measurements agree with those in the literature from the host galaxies.

The precise calibration of astrophysical properties using a single measurement epoch, as in several of these SNe, can be a powerful advantage of the EPM over other techniques, where the observations need not only to be densely sampled but also require concurrent multi-band photometry. Given the potential challenges of observing with large pitch, unfiltered CCDs, the measurements in Fig. 10 are remarkably linear thru the entire range of epochs chosen for all of the SNe in this sample. Dense sampling during the plateau phase increases statistics and could reduce the EPM uncertainties. However, the low scatter of points around these slopes, which arises in part from the low scatter of points around the physical parameter evolution models, suggests observables have strong correlations and numerous concurrent observations are not absolutely necessary for the EPM measurements.

These results strongly suggest a robustness of the method to the choice of plateau span utilized. In particular, stripped core supernovae of types Ib and Ic that lack extensive plateaus might be viable in this method using a shorter time duration. Such a possibility was already explored in Vinkó et al. (2004) with SN 2002ap. We have also obtained a preliminary result for 2007gr in Staten (2020). Both yielded distances to their hosts in agreement with the literature.

Our analysis shows an inherent promise of the EPM method whose very general physical assumptions have allowed us to leverage unfiltered photometry with minimal spectroscopy and color information. In fact, the results indicate that SNe with only one epoch of either performed similarly to those with 3 or more epochs when using the normalized, exponential time evolution models described in Section 5. Our results can also be obtained by using V band photometry in place of the unfiltered photometry. We note that while the accurate systematics from the dilution parameter may affect the distance results, some limitation in their magnitude can be inferred from the linearity of the EPM plots over the whole plateau, and by the validity of the SNe IIP distances compared to their host's. Further work, where the uncertainties will be reduced overall, will necessitate more careful handling of this issue. Fig 13 shows the EPM distance

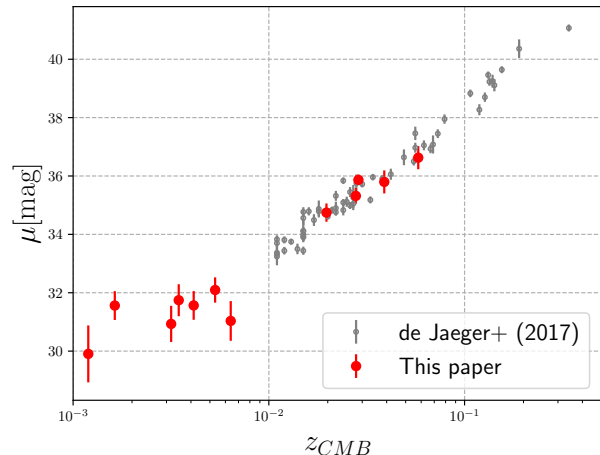


FIG. 13.— Distance moduli for the 12 SNe in our sample using the EPM method are overlaid on top of the SCM measurements from de Jaeger et al. (2017). The distance uncertainties for our sample include the contribution from flat peculiar velocity of 300 km s^{-1} along with the statistical and total uncorrelated uncertainties from Table 3, added in quadrature.

modulus derived for our SN sample overlaid on top of those measured from the SCM technique by de Jaeger et al. (2017) (see Fig. 5 in their paper). On the overlapping redshift range, the distances measured from independent methods and samples are statistically consistent.

A driving motivation in the current study was to test cosmic expansion in the local universe. The linear method we used has the advantage that it makes no cosmological assumption and allowed us to estimate and mitigate the effects from peculiar motion via a simple simulation. As such, it yielded consistent values of $H_0 = 67.4 \pm 11.8(\text{stat.}) \text{ km s}^{-1} \text{ Mpc}^{-1}$ and $H_0 = 75.6 \pm 5.1(\text{stat.}) \pm 0.3(\text{syst.}) \text{ km s}^{-1} \text{ Mpc}^{-1}$ in the *local* and *H - flow* regimes, respectively, with very different relative sizes of peculiar velocities to cosmic recession. The combined measurement yields $H_0 = 74.3^{+4.7}_{-4.7}(\text{stat.})^{+4.1}_{-3.7}(\text{syst.}) \pm 0.3 (\text{Pec. Vel.}) \text{ km s}^{-1} \text{ Mpc}^{-1}$. The impact of peculiar velocities is minimal. We can also see that with only 12 SNe, we are already almost systematics dominated. Future work will require more effort to reduce systematic effects.

The MCMC method we employed presented different advantages to the analysis. The technique jointly estimates the posterior distribution for H_0 and a measure of intrinsic residual systematic uncertainty σ_{int} for the analysis. We utilize the full information in the covariance matrix, and the approach provides a test of unknown contributions to the scatter of points. The value returned, corresponding to $0.3^{+0.42}_{-0.26} \text{ Mpc}$ is consistent with zero. We obtain a measurement for the full sample of 12 SNe of $H_0 = 72.9^{+5.7}_{-4.3} \text{ km s}^{-1} \text{ Mpc}^{-1}$, which is in excellent agreement with the result from the linear method. Even though we have fixed other cosmological parameters, it is interesting to note that the residual intrinsic dispersion we find from the analysis of our SNe IIP sample is not statistically significant.

For a quick test, we repeated the MCMC analysis using the 5 events from the $z > 0.01$ sample but dropping

the peculiar velocity from the uncorrelated diagonal error term. This choice of cutoff is ubiquitous in the literature including the SNe Ia studies. The contribution from the galactic peculiar motion at such redshift is expected to be $\sim 10\%$ or less (e.g. Kessler et al. (2009)). In such a limited sample, we observe no statistically significant shift in either H_0 or σ_{int} . Because we incorporated the correlated systematic uncertainties within the covariance matrix of the distances in the MCMC analysis, we take this estimate as our final estimation for H_0 .

When comparing to the other probes such as SNe Ia measurements from recent DES results (Abbott et al. (2019)), we see that our results are in good agreement. We also find our estimated H_0 value to be consistent with that obtained from the CMB measurements (Planck Collaboration et al. (2016)) at the 1σ level. In the future, our measurement can be substantially improved by a larger sample, and by more careful consideration of the underlying time evolution modeling and correlations among SNe we have utilized.

9. CONCLUSION

We performed an end to end analysis of time evolution of SNe IIP properties and of cosmological properties measurement in the EPM framework using photometric and spectroscopic observations of a sample of 12 SNe IIP. We significantly improved the ROTSE SNe photometry sampling and precision with new image differencing for ROTSE SNe images using a kernel convolution technique.

In our analysis of SNe IIP, we have established excellent performance of unfiltered CCD photometry, including in areas crowded by host nuclei, to yield valuable measurements of supernova properties and to measure cosmic expansion in the nearby universe. We demonstrated a broad consistency between SNe IIP of the time

evolution of event ejecta velocities and photospheric temperatures from the times of peak luminosity throughout most of the plateau among these diverse SNe. We empirically established parametric evolution models to extrapolate the photospheric velocity and temperature from as few as a single photometric and spectroscopic measurement. Using the EPM technique, we obtained the luminosity distances for each SN. These distance measurements are in good agreement with host distances in the literature, and the linearity of the EPM diagrams suggests the viability of further generalization of this approach. Overall, the EPM technique looks promising to pursue cosmological studies for larger data sets, potentially to even higher red shifts.

Utilizing two approaches to fitting for H_0 , we have obtained a measurement of $H_0 = 72.9^{+5.7}_{-4.3}$ kms $^{-1}$ Mpc $^{-1}$. We further established that unknown peculiar velocities do not significantly impact this measurement. Results from an MCMC approach also indicate that we have accounted for all appreciable contributors, and their uncertainties to the scatter of points.

10. ACKNOWLEDGEMENT

RK wishes to thank NASA grant NNX10A196H (P.I. Kehoe), and SMUs Deans Research Council, for supporting the initial work for this paper. JCW and JV are supported in part by NSF AST-1813825. JV and his group at Konkoly Observatory are supported by the project ‘‘Transient Astrophysical Objects’’ GINOP 2.3.2-15-2016-00033 of the National Research, Development and Innovation Office (NKFIH), Hungary, funded by the European Union. We would like to acknowledge the McDonald Observatory technical and observation support crew for tremendous help during the ROTSE and HET observations over the years. We would like to thank Jeffrey Silverman for useful discussions on the data processing and analysis.

REFERENCES

- Abbott, T. M. C., Allam, S., Andersen, P., et al. 2019, *ApJ*, 872, L30. doi:10.3847/2041-8213/ab04fa
- Akerlof, C. W., Kehoe, R. L., McKay, T. A., et al. 2003, *PASP*, 115, 132
- Alard, C., & Lupton, R. H. 1998, *ApJ*, 503, 325
- D’Andrea, C. B., Sako, M., Dilday, B., et al. 2010, *ApJ*, 708, 661
- Bailey, S. 2012, *PASP*, 124, 1015
- Becker, A. C., Homrighausen, D., Connolly, A. J., et al. 2012, *MNRAS*, 425, 1341
- Benetti, S., Cappellaro, E., Mazzali, P. A., et al. 2005, *ApJ*, 623, 1011
- Bertin, E. & Arnouts, S. 1996, *A&AS*, 117, 393. doi:10.1051/aas:1996164
- Blondin, S., Dessart, L., Hillier, D. J., et al. 2017, *MNRAS*, 470, 157. doi:10.1093/mnras/stw2492
- Bolton, A. S., & Schlegel, D. J. 2010, *PASP*, 122, 248
- Bose, S., & Kumar, B. 2014, *ApJ*, 782, 98
- Bose, S., Valenti, S., Misra, K., et al. 2015, *MNRAS*, 450, 2373
- Bramich, D. M. 2008, *MNRAS*, 386, L77
- Branch, D., & Wheeler, J. C. 2017, *Supernova Explosions: Astronomy and Astrophysics Library*
- Broun, D., Scolnic, D., Popovic, B., et al. 2022, *ApJ*, 938, 110. doi:10.3847/1538-4357/ac8e04
- DES Collaboration et al. 2018 *Phys. Rev. Lett.*, 122, 171301
- Dessart, L., & Hillier, D. J. 2005, *A&A* 439, 671
- de Jaeger, T., González-Gaitán, S., Anderson, J. P., et al. 2015, *ApJ*, 815, 121
- de Jaeger, T., Galbany, L., Filippenko, A. V., et al. 2017, *MNRAS*, 472, 4233
- Dhungana, G., Kehoe, R., Vinko, J., et al. 2016, *ApJ*, 822, 6
- Dhungana, G. 2018, Ph.D. Thesis; Southern Methodist University, Dallas, TX, USA
- Davis, T. M., Hui, L., Frieman, J. A., et al. 2011, *ApJ*, 741, 67
- Dong, Y., Valenti, S., Bostroem, K. A., et al. 2021, *ApJ*, 906, 56. doi:10.3847/1538-4357/abc417
- Eastman, R. G., Schmidt, B. P., & Kirshner, R. 1996, *ApJ*, 466, 911
- Elmhamdi, A., Tsvetkov, D., Danziger, I. J., & Kordi, A. 2011, *ApJ*, 731, 129
- Faran, T., Poznanski, D., Filippenko, A. V., et al. 2014, *MNRAS*, 442, 844
- Filippenko, A. V. 1997, *ARA&A*, 35, 309
- Fitzpatrick, E. L. 1999, *PASP*, 111, 63
- Foreman-Mackey, D., Hogg, D. W., Lang, D., & Goodman, J. 2013, *PASP*, 125, 306
- Gall, E. E. E., Kotak, R., Leibundgut, B., et al. 2016, *A&A*, 592, A129 Gall et al. (2017)
- Gall, E. E. E., Kotak, R., Leibundgut, B., et al. 2018, *A&A*, 611, A25. doi:10.1051/0004-6361/201731271
- Graur, O., Bianco, F. B., & Modjaz, M. 2015, *MNRAS*, 450, 905
- Graziani, R., Courtois, H. M., Lavaux, et al. 2019, *MNRAS*, 488, 4
- Guillochon, J., Parrent, J., Kelley, L. Z., & Margutti, R. 2017, *ApJ*, 835, 64
- Gal-Yam, A., Bufano, F., Barlow, T. A., et al. 2008, *ApJ*, 685, L117
- Hatano, K., Branch, D., Fisher, A., et al. 1999, *ApJS*, 121, 233
- Hamuy, M., & Pinto, P. A. 2002, *ApJ*, 566, 63

- Hamuy, M., Pinto, P. A., Maza, J., et al. 2001, *ApJ*, 558, 615
- Hill, G. J., Nicklas, H. E., MacQueen, P. J., et al. 1998, *Society of Photo-Optical Instrumentation Engineers (SPIE) Conference Series*, 3355, 375
- Howell, D. A. 2011, *Nature Communications*, 2, 350
- Johnson, A., Blake, C. Koda, J. et al. 2014, *MNRAS*, 444, 4
- Jones, M. I., Hamuy, M., Lira, P., et al. 2009, *ApJ*, 696, 1176
- Kasen, D., & Woosley, S. E. 2009, *ApJ*, 703, 2205
- Kessler, R., Becker, A. C., Cinabro, D., et al. 2009, *ApJS*, 185, 32
- Kessler, R., Marriner, J., Childress, M., et al. 2015, *AJ*, 150, 172
- Kelly, P. L., & Kirshner, R. P. 2012, *ApJ*, 759, 107
- Khazov, D., Yaron, O., Gal-Yam, A., et al. 2016, *ApJ*, 818, 3
- Kirshner, R. P., & Kwan, J. 1974, *ApJ*, 193, 27
- 2002PASP...114...35L Leonard, D. C., Filippenko, A. V., Gates, E. L., et al. 2002, *PASP*, 114, 35
- Marion, G. H., Brown, P. J., Vinkó, J., et al. 2016, *ApJ*, 820, 92
- Nicola, A., Refregier, A., & Amara, A. 2017, *Phys. Rev. D*, 95, 083523. doi:10.1103/PhysRevD.95.083523
- Nugent, P. E., Sullivan, M., Ellis, R., et al. 2006, *ApJ*, 645, 841
- Pedregosa, F., Varoquaux, G., Gramfort, A., et al. 2012, arXiv:1201.0490
- Pejcha, O. & Prieto, J. L. 2015, *ApJ*, 799, 215. doi:10.1088/0004-637X/799/2/215
- Perlmutter, S., Aldering, G., Goldhaber, G., et al. 1999, *ApJ*, 517, 565
- Phillips, M. M. 1993, *ApJ*, 413, L105
- Planck Collaboration, Ade, P. A. R., Aghanim, N., et al. 2016, *A&A*, 594, A13. doi:10.1051/0004-6361/201525830
- Poznanski, D., Nugent, P. E., & Filippenko, A. V. 2010, *ApJ*, 721, 956
- Quimby, R. M., Wheeler, J. C., Höflich, P., et al. 2007, *ApJ*, 666, 1093
- Quimby, R. M. 2006, Ph.D. Thesis, University of Texas, Austin, TX, USA
- Riess, A. G., Filippenko, A. V., Challis, P., et al. 1998, *AJ*, 116, 1009
- Rodríguez, Ó., Clocchiatti, A., & Hamuy, M. 2014, *AJ*, 148, 107
- Rodríguez, Ó., Pignata, G., Hamuy, M., et al. 2019, *MNRAS*, 483, 5459
- Roy, R., Kumar, B., Benetti, S., et al. 2011, *ApJ*, 736, 76
- Schlafly, E. F., & Finkbeiner, D. P. 2011, *ApJ*, 737, 103
- Schmidt, B. P., Kirshner, R. P., Eastman, R. G., et al. 1994, *ApJ*, 432, 42
- Silverman, J. M., Foley, R. J., Filippenko, A. V., et al. 2012, *MNRAS*, 425, 1789 Szalai et al. (2019)
- Staten, R. 2020, Ph.D. Thesis; Southern Methodist University, Dallas, TX, USA
- Szalai, T., Vinkó, J., Könyves-Tóth, R., et al. 2019, *ApJ*, 876, 19. doi:10.3847/1538-4357/ab12d0
- Tripp, R. 1998, *A&A*, 331, 815
- Valenti, S., Sand, D., Stritzinger, M., et al. 2015, *MNRAS*, 448, 2608
- Valenti, S., Howell, D. A., Stritzinger, M. D., et al. 2016, *MNRAS*, 459, 3939
- Van Dyk, S. D., Zheng, W., Maund, J. R., et al. 2019, *ApJ*, 875, 136. doi:10.3847/1538-4357/ab1136
- Vinkó, J., Blake, R. M., Sárneczky, K., et al. 2004, *A&A*, 427, 453. doi:10.1051/0004-6361:20040272
- Vinkó, J., Takáts, K., Szalai, T., et al. 2012, *A&A*, 540, A93
- Vogl, C., Sim, S. A., Noebauer, U. M., et al. 2019, *A&A*, 621, A29. doi:10.1051/0004-6361/201833701
- Weinberg, D. H., Mortonson, M. J., Eisenstein, D. J., et al. 2013, *Phys. Rep.*, 530, 87W
- Yaron, O., & Gal-Yam, A. 2012, *PASP*, 124, 668
- Yuan, F., & Akerlof, C. 2008, *ApJ*, 677, 808
- Yuan, F. 2010, Ph.D. Thesis; University of Michigan, Ann Arbor, MI, USA